

Using a Radical Scavenger and Modeling the Improvement of Linewidth in One-Photon Direct Laser Writing Lithography

A Senior Project submitted to
The Division of Science, Mathematics, and Computing
of
Bard College

by
Shuyi WENG
翁舒逸

Annandale-on-Hudson, New York
May, 2014

Dedication

TO MY MOM

致母亲

Acknowledgements

This project would not have been completed without the help and support from my professors, friends, and family members. I would like to offer my special thanks to my project advisors, Dr. Christopher LaFratta and Dr. Csilla Szabo, for their helpful suggestions, careful supervision, and inspiring guidance in both realms of chemistry and mathematics. I am particularly grateful for the assistance given by my academic advisor, Dr. Emily McLaughlin, who inspired me with the idea of radical scavenging with knowledge from organic chemistry. I would also like to thank Dr. Jennie D'Ambroise, for her suggestion of using segmented PDEs to approach the modeling. I wish to acknowledge the assistance provided by my lab peers Olja Simoska, Ian Pelse, Miles Ingram, Zhe Mei, Min Kyung Shinn, Jasper Williams, Ingrid Stolt, and Clare Wheeler, as well as all the other chemistry seniors. The constant support from my friends Seo Young Kim, Yan Chu, Yushan Jiang, Zexi Song, Jin Zhang, Xujun Liu, and Thinh Pham, has also been a great pushing force for my work. Last but not least, I would like to thank my family members for their care and support on me, even though hardships have struck us harshly in the past year.

Abstract

Direct laser writing (DLW) lithography is a useful way to generate microscopic patterns for lab-on-a-chip devices. We have developed a simple and inexpensive platform for the creation of these initial patterns using a homemade acrylic resin, a 405-nm laser diode, and a fluorescence microscope. To create sub-micrometer linewidths, we included a radical scavenger in the photoresist to quench excessive amounts of radicals generated from laser exposure. In this project, we compared various formulations of the photoresist and we presented a model for the radical polymerization in our photoresist. The model utilized the method of finite differences to numerically solve a system of parabolic partial differential equations describing the diffusive behaviors of particles in the photoresist. The model also made use of Markov chains to simulate the step-wise polymerization of the photoresist. The parameters in the model were determined by fitting the model on experimentally-obtained data.

Contents

Dedication	i
Acknowledgements	ii
Abstract	iii

I Laboratory Experiments

1 Introduction I	2
1.1 Photolithography	4
1.2 Direct Laser Writing (DLW)	5
1.3 Acrylic Ester Polymerization	8
1.4 Memory Effect	9
1.5 Radical Inhibition	11
2 Experimental Overview	12
2.1 Laser Setup	13
2.2 Microscope and Automated Stage	15
2.3 Photoresist	17
2.4 Modified Glass Slides or Coverslips	19
2.5 Constructing a Micro-Scale Structure	19

2.6	Developing a Micro-Scale Structure	22
2.7	Scanning Electron Microscopy (SEM)	22
3	Shrinkage Study	23
3.1	Methods	24
3.2	Results	25
3.3	Discussion	28
4	Linewidth Characterization	29
4.1	Methods	29
4.2	Results	31
4.3	Discussion	31
II	Mathematical Modeling	
5	Introduction II	36
5.1	The Gaussian Beam	37
5.2	Parabolic Equations	40
5.3	Method of Finite Differences	43
5.4	Markov Chains	45
6	Memory Effect Characterization	48
6.1	Oscilloscope Setup	49
6.2	Methods	49
6.3	Results	51
6.4	Discussion	53
7	Modeling the Memory Effect	54
7.1	First Approximation: Radical Initiation	56
7.2	Second Approximation: Acrylate Initiation	59

7.3	Probability of Polymerization	61
7.4	Third Approximation: Markov Modeling	63
8	Mathematica Implementation	65
8.1	Finite Difference Modeling	65
8.2	Markov Modeling	66
8.3	Pseudocode for the Implementation	67
8.4	Results and Discussion	69
8.5	Future Development	73
A	Linewidths before/after Alcohol Development	75
B	Linewidth Data with Different DLW Conditions	82
C	SEM Images of Double Dots	88
D	Coding in Mathematica	93
D.1	Parameters	93
D.2	Initial Conditions	94
D.3	First Exposure	95
D.4	Second Exposure	97
D.5	Showing the Result	99
E	Sample Simulation	100
F	General Solutions to $y' = ky(1 - y)$	104

List of Figures

1.1	Photoinitiator Absorption	6
1.2	Laser Beam Going through the Photoresist	7
1.3	Acrylic Acid and Acrylic Ester	8
1.4	Acrylic Ester Polymerization	9
1.5	Example of “Memory Effect”	10
1.6	Inhibition Mechanism	11
2.1	Laser Schematic	13
2.2	Comparison between Airy Disk and Gaussian Function	15
2.3	Microscope Schematic	15
2.4	Direct Laser Writing Setup	16
2.5	Photoresist Composition	17
2.6	Hybrid Structure	21
3.1	Shrinkage Comparison	23
3.2	Structure Used to Measure the Shrinkage Coefficient	25
3.3	Waffle Structure and Measuring Scheme	27
4.1	Straight Lines for Linewidth Measurements	30
4.2	Linewidth of DLW	32
4.3	Linewidths under 150 nW, 20 μ m/s (after shrinkage)	34

4.4 Linewidths under 150 nW, $20\mu\text{m}/\text{s}$ (before shrinkage)	34
5.1 Beam Radius as a Function of z	39
5.2 Difference Grid on the Space-Time Domain	44
5.3 A State Diagram of the Markov Chain for Directional Random Walk . . .	46
6.1 Digital oscilloscope	49
6.2 Merged Double-Dot	51
7.1 Beam Intensity and Reflection Intensity	58
7.2 Modeling the Probability Function	62
8.1 Simulation Result of Experiment #2	71
8.2 Final State of Simulation #8	72

List of Tables

2.1	Composition of Different Photoresists	18
3.1	Percent Shrinkage of Photoresists	26
3.2	Shrinkage in Microscale	27
4.1	Laser Powers and Writing Speeds for Linewidth Characterization	30
4.2	Calculated Linewidths	34
6.1	Base Speed Range for Specific Hiatus Time	50
6.2	Memory Effect Measurements	52
7.1	Table of Variables and Coefficients	55
7.2	Table of Functions and Lists	56
8.1	Choices for Parameters and Functions	69
8.2	Percent Increase Results Simulated by the Model	70
8.3	Comparison between Experiments and the Model	72
A.1	Shrinkage Characterization for Photoresist #1	76
A.2	Shrinkage Characterization for Photoresist #2	76
A.3	Shrinkage Characterization for Photoresist #3	77
A.4	Shrinkage Characterization for Photoresist #4	77
B.1	Linewidth Measurement for Photoresist #1	83

B.2 Linewidth Measurement for Photoresist #2	84
B.3 Linewidth Measurement for Photoresist #3	85
B.4 Linewidth Measurement for Photoresist #4	86
B.5 Linewidth under Different Condition	87

Part I

Laboratory Experiments

Chapter 1

Introduction I

The rapid development of science and technology has demanded the construction of smaller and smaller structures for various reasons. In the realm of computer engineering, *Moore's Law* [Moo65], proposed in 1965, accurately predicted that the number of transistors on an integrated circuit would double approximately every two years. In order for millions and even billions of transistors to be created on a single chip, their size has to be miniature. The shrinking of electronics components and their integration into complex circuits have enabled the creation of modern electronics and the age of information.

A similar miniaturization revolution is underway in the physical sciences. First predicted by the physicist Richard Feynman in his famous “There’s plenty of room at the bottom” lecture, Feynman explains the basic tenets of nanotechnology. The fields of chemistry and biology are joining physics and the electronics industry in trying to make technologies smaller, faster, and cheaper. For example, the assays on micro-biological

structures require testing chambers of the size comparable to a single bacterium or a red blood cell [ZNWS13, TBP⁺11], which is usually in *micrometer* scale. The demands on micro-structures from biological sciences have given rise to the development of micro total analysis systems (μ TAS) [KOM⁺13], which integrate the functionalities of multiple chemical assays into one single chip. Such devices are known as “lab-on-a-chip” (LOC) for their capability to perform various chemical tests and their ability to operate assays using only picoliters of sample.

The use of micro-scale devices is constantly increasing in chemistry and biology, and so the study of new fabrication techniques is an ever evolving and important field. Nowadays in electronics industry, photolithography has become one of the most commonly-applied techniques for microfabrication [Jae02]. It uses a mask to expose the surface of a layer of photoresist selectively by ultraviolet (UV) light, chemically changing the photoresist such that the exposed area is more or less soluble than the unexposed area. After development in a solvent, a two-dimensional pattern is left on the substrate. With multiple runs of such processes, a complicated circuit system can be “drawn” on the substrate. Besides photolithography, other techniques for the fabrication of micro-structures include electron beam lithography [RC97], dynamic masking [IKT⁺08], high precision machining [ZRM⁺03], and direct laser writing. One of the main distinctions between these methods and conventional mask-based lithography is their serial nature compared to the parallel nature of masks.

1.1 Photolithography

Conventional mask-based photolithography is widely practiced in contemporary electronics industry. A series of sophisticated manipulations are performed under highly-regulated conditions [Jae02] to produce integrated circuits that go into commercial computer chips and processors.

The whole process of photolithography takes place in a clean room. It transfers patterns from masks to photoresist on the surface of silicon wafers. Commercial chips are mostly produced on silicon wafers with *positive* photoresists, in which case the area exposed under UV light turns soluble and can be washed off by solvents. In the subsequent etching or doping steps, the photoresist protects portions of the surface while windows are etched in barrier layer such as silicon dioxide, silicon nitride, or metal. After etching, the photoresist is removed, and impurities can be introduced into the wafer through the windows, or metal can be deposited on the surface making contact with the silicon through the etched windows.

Photolithography requires the use of photomasks at the ultraviolet exposure step. One photomask gives only a specific pattern on the wafer, while that pattern may contain millions of features that are all made in parallel. Multiple photomasks are required for different structures drawn on the substrate, which could be inconvenient and expensive. Hence, some maskless alternatives have been developed to overcome the drawbacks of photolithography.

1.2 Direct Laser Writing (DLW)

Direct laser writing (DLW) is an effective way to fabricate micro-structures without a mask. It uses a moving laser to initiate a change in the solubility of the photoresist to achieve its goal. Similar with those in photolithography, the photoresists used in DLW can be either positive or negative. Usually in DLW, a *negative* photoresist consists of at least a monomer and a photoinitiator. The photoinitiator absorbs photonic energy from the laser, breaks apart into radicals, and initiates the polymerization process. Depending on the type of photonic absorption by the photoinitiator, DLW can be categorized into two major branches: one-photon DLW and two-photon DLW. The free radicals generated by the photoinitiator subsequently trigger the polymerization reaction of the monomers, which will be further discussed in section 1.3.

1.2.1 One-photon DLW

Photoinitiators are usually capable of homolytic cleavage at one or more of its chemical bonds, resulting in the formation of free radicals (Figure 1.1). When a photoinitiator molecule absorbs a photon with a specific range of wavelengths, the molecule is excited from the ground state (S_0) to an excited electronic state (S_1^*). The molecule then undergoes non-radiative relaxation into the vibrational ground state of the first excited state (S_1). Intersystem crossing (ISC) occurs at this moment to bring the molecule from a singlet state (S_1) to a triplet state (T_1). The molecules in the triplet state are classically

forbidden to make the transition back to the ground state, which makes the lifetime of excited molecules long enough to yield free radicals.

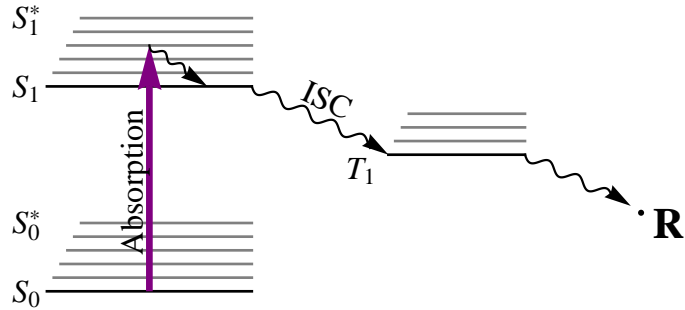


Figure 1.1: A Jablonski Diagram Showing the Activation of the Photoinitiator

1.2.2 Two-photon DLW

Normally, a molecule absorbs only one photon to make transitions between its electronic states. However, when two photons hit a molecule *simultaneously* (which rarely happens in nature because the photon intensity required is extremely high), the molecule is able to make a transition to an excited state with an energy gap corresponding to the energy sum of these two photons [Abe62]. Such a process is usually achieved with pulsed lasers, which produce pulses with high intensity. The highly intense laser pulses make two-photon absorption possible in a tiny volume element, or *voxel*, at the focal point of the laser, thus generating a limited amount of free radicals that are only able to polymerize the photoresist at this small scale.

1.2.3 Comparisons between the two types of DLW

In contemporary research labs, both one-photon DLW and two-photon DLW techniques are practiced for their distinctive advantages over one another.

Two-photon DLW gives structures with smaller linewidths and resolution comparing to one-photon DLW. When the laser beam is focused on the surface of the substrate (Figure 1.2), it goes through the photoresist, and the intensity of the beam decreases proportional to the square of the distance from the focal point. In one-photon DLW, a large range of beam intensity is capable for photoinitiation and polymerization. Even a low beam intensity leads to a low concentration of free radicals, which may not reach the level required for polymerization, but enough to generate oligomers that turns into polymer more easily and more rapidly than unexposed photoresist. However, in two-photon DLW, the beam intensity plays an important role in the initiation process. For two photons to reach one photoinitiator molecule *simultaneously*, a high intensity of the laser beam

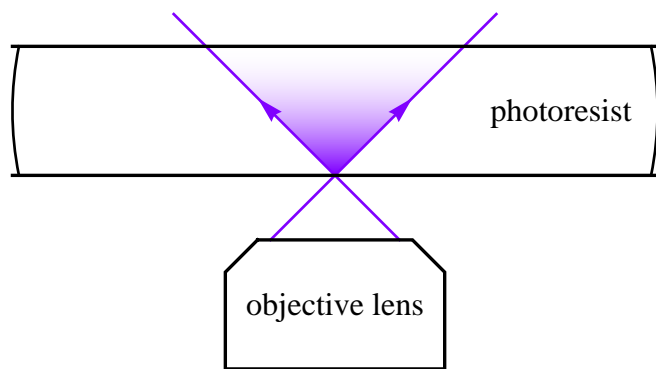


Figure 1.2: Laser beam going through the photoresist, with the gradient illustrating change in beam intensity

is required. Such high intensity is only attained near the focal point, while further away from the focal point, the probability for two photons to reach the same molecule at the same time is essentially zero. Thus the free radicals are only generated within a short distance of the focus but not deep into the photoresist. The highly-localized radicals in two-photon DLW yield smaller structures with higher resolutions than one-photon DLW does.

However, the cost for a pulsed laser used in two-photon DLW is much higher than that of a continuous wave laser. A femtosecond titanium:sapphire laser used in two-photon DLW costs more than \$100,000 together with a 532-nm pump laser, while a 405-nm laser diode module is available at \$185 on ThorLabs®.

1.3 Acrylic Ester Polymerization

Acrylic esters (Figure 1.3) are the most commonly-used monomers in DLW photoresists. They undergo radical polymerization when a photoinitiator is used to generate radicals. The reaction mechanism is shown in Figure 1.4.

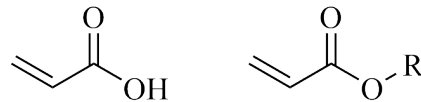


Figure 1.3: Acrylic Acid and Acrylic esters

The introduction of multiple acrylate groups in the R chain of the acrylic ester molecule leads to branching and cross-linking of polymer chains, thus enhancing the strength and

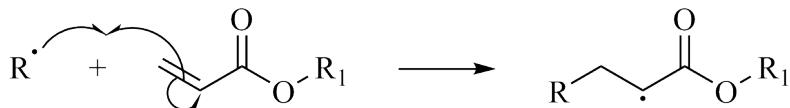
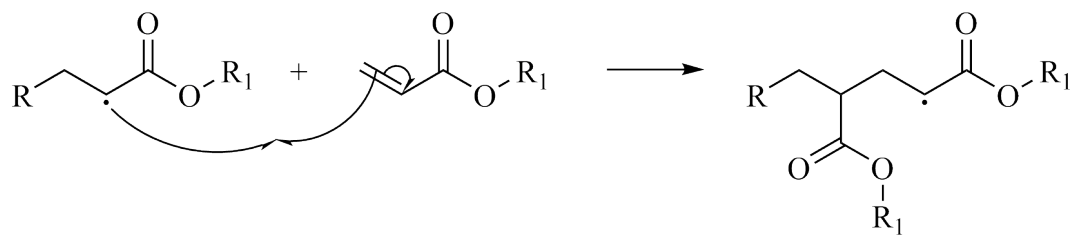
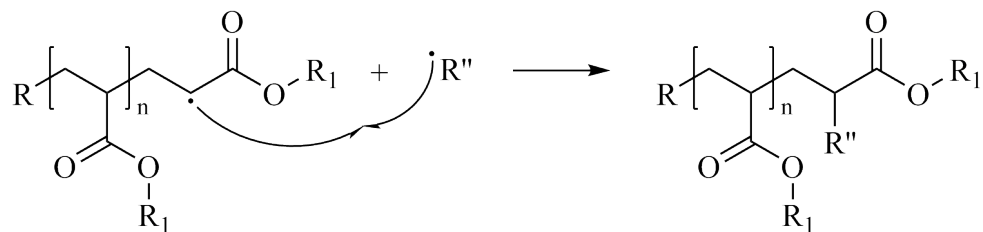
Radical Initiation:**Chain Initiation:****Chain Propagation:****Chain Termination:**

Figure 1.4: A Mechanism for Acrylic Ester Polymerization

rigidity of the polymer. Substances with multiple acrylate groups are often used in DLW as the monomer [FW13].

1.4 Memory Effect

As shown in Figure 1.2, the beam intensity decreases as the laser beam goes deeper into the photoresist. The beam intensity reaches its maximum at the focus, promoting

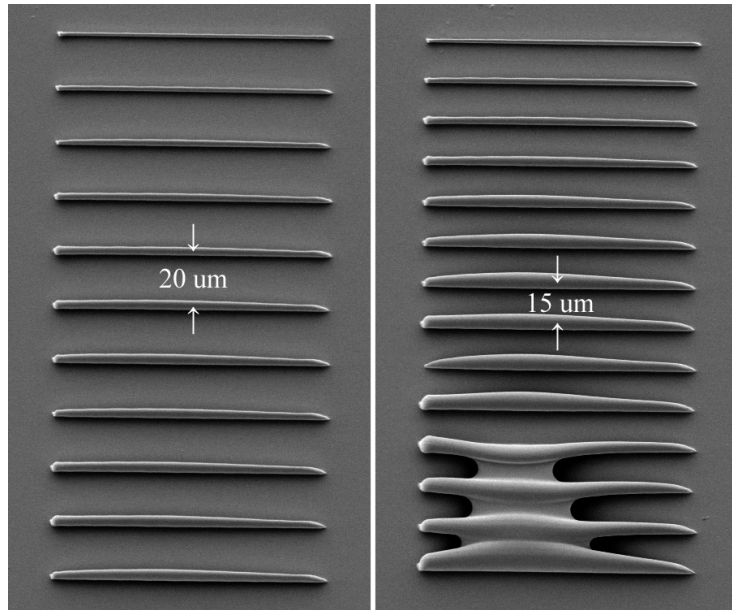


Figure 1.5: An example of “memory effect”, where the lines are drawn from top to bottom

the radical initiation at that point, but photons are also absorbed beyond the focal point. The concentration of initiated free radicals beyond the focal point may not be high enough to propagate the growth of long-chain polymers, but the generated radicals do not die off immediately, and the oligomer molecules linger. The lifetime of the radicals is long enough to affect the subsequent exposures nearby, resulting in an increase in linewidth of the structures (Figure 1.5). Additionally, the photoresist, while quite viscous, does allow for diffusion of radicals, and the reflection of the laser beam within the photoresist also leads to higher-order exposure. The diffusion of radicals and smaller oligomers made unintentionally beyond the focal point affect the resolution of DLW, and thus prohibit the fabrication of structures as small or as close to each other as we wish. Since it usually appears to us that the photoresist somehow “remembers” previous laser exposures and

affects nearby structures fabricated a short time later, we have named this phenomenon the “memory effect”.

1.5 Radical Inhibition

Radical scavengers are commonly used in chemistry in order to remove or deactivate unwanted reaction products in a mixture. For example, butylated hydroxytoluene (BHT) is usually added to the stock of diethyl ether as an inhibitor [Sig13] to prevent the formation of explosive diethyl ether hydroperoxide, which reacts via a radical pathway.

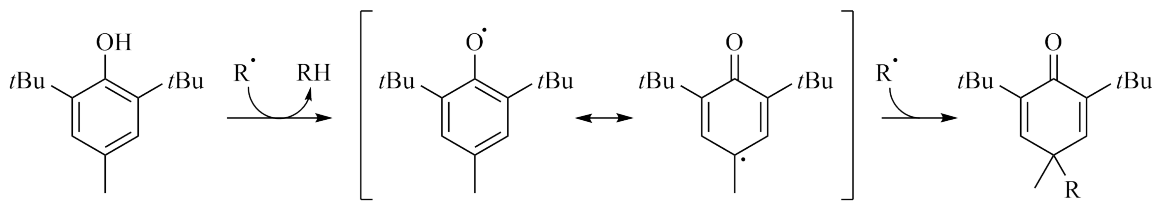


Figure 1.6: The Mechanism for Radical Inhibition with BHT

The polymerization of monomers depends on the concentration of free radicals in the photoresist, and here is where the idea of inhibition comes from. One-photon DLW creates unwanted free radicals and unpolymerized oligomer molecules beyond the focal point after each exposure. If radical scavengers are added into the photoresist, they will be able to quench the free radicals, thus preventing further polymerization involving these free radicals and improving linewidth and resolution in one-photon DLW.

Chapter 2

Experimental Overview

The fabrication of micro-scale structures is carried out with a systematic procedure. The procedure starts from modifying glass slides or coverslips. Acrylate groups are attached to the surface of the glass substrate so that the polymerized photoresist may bond tightly to the glass surface. The photoresist in our experiments consists of three substances - the monomer, photoinitiator, and the radical scavenger. When a collimated laser beam is focused onto the photoresist, the photoinitiator is excited and turns into radicals, initiating the radical polymerization process as shown in Figure 1.4. The laser beam is filtered and collimated by a series of optics carefully positioned on an optical table equipped with vibration isolation system. The glass slide with photoresist is fixed on an automated stage that moves in the plane perpendicular to the laser beam. Polymer structures are fabricated by moving the stage relative to the laser beam, leaving polymers attached on the modified glass surface.

In the following sections, descriptions of each experimental procedure and apparatuses in use are provided in detail.

2.1 Laser Setup

A laser diode module (CPS405, ThorLabs, USA) is used throughout our experiments. It produces a 405-nm, 4.5-mW elliptical beam. However, a collimated circular beam is desired for our purposes. Therefore, two converging lenses and a pinhole are installed together with a few other optical equipments to modulate the beam, as shown in Figure 2.1.

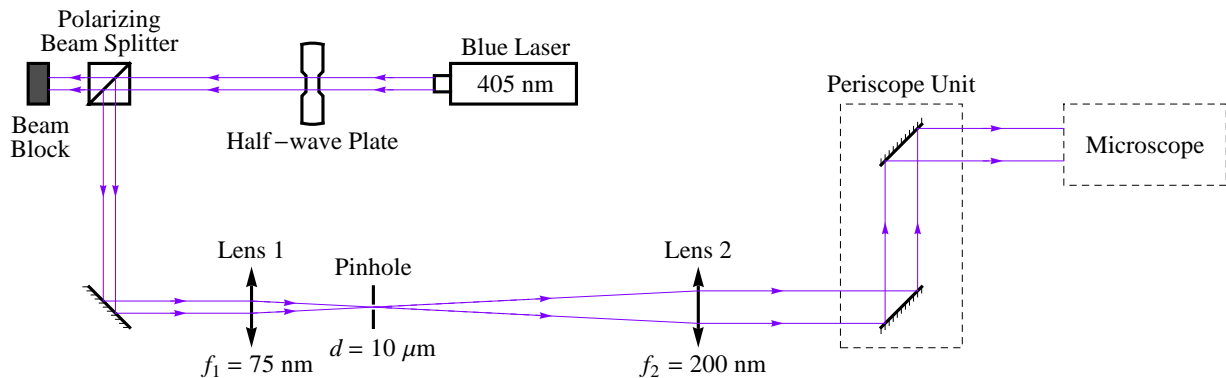


Figure 2.1: A schematic for the collimation of the laser

The beam coming out of the laser diode is plane polarized. The half-wave plate is a birefringent crystal that rotates the plane of polarization when the crystal is rotated. Different polarization of the beam results in different amount of reflection from the polarizing beam splitter. The combination of these two pieces of equipment allows us to efficiently control the power output by rotating the half-wave plate.

The lenses in this system are placed in a way such that the principle axes of the two lenses align with the center of the laser beam, and the distance between them equals the sum of their focal distance. In this fashion, a telescope that expands and collimates the beam is created. A pinhole of diameter $10 \mu\text{m}$ is placed at the common focal point of the lenses. This pinhole acts as a spatial filter to remove unwanted transverse laser modes. This arrangement results in an output pattern of an Airy disk [Air35, ST91]. The intensity of the Airy disk is symmetric around its center, and the relation between the intensity and the distance from the center can be expressed in terms of the Bessel function:

$$I(\theta) = I_0 \left(\frac{2J_1(ka \sin \theta)}{ka \sin \theta} \right)^2,$$

where I_0 is the intensity at the center, $k = 2\pi/\lambda$ is the wavenumber, a is the radius of the pinhole, and J_1 is the Bessel function of the first kind of order one. If we let $x = ka \sin \theta$, and plot $I(x)/I_0$, we may discover that it resembles the curve for a Gaussian function (Figure 2.2). In fact, in Part II of this project, we are going to approximate the laser beam as a Gaussian beam. All the results of mathematical modeling in this project are based on this approximation.

Once the laser beam passes through the lenses and the pinhole, it is considered nicely circular and collimated. The beam is now ready to enter the microscope for DLW. The periscope unit consists of two mirrors that change the direction of the beam and send it up into the microscope.

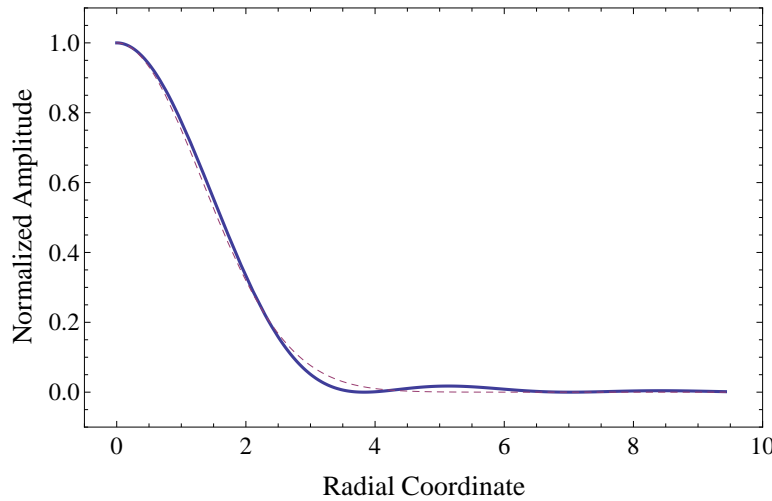


Figure 2.2: Comparison between the intensity of Airy disk and Gaussian function

2.2 Microscope and Automated Stage

The collimated beam is first reflected by a dichroic mirror after it enters the microscope unit. The dichroic mirror reflects wavelengths less than 420 nm and transmits longer

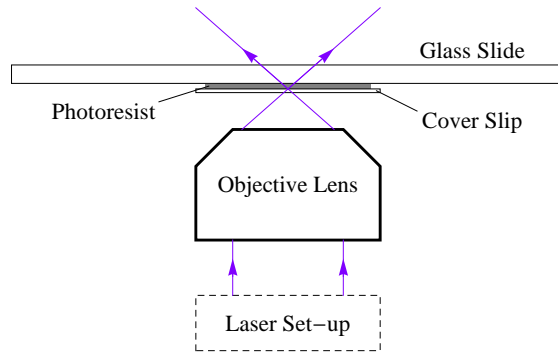


Figure 2.3: A schematic for the collimated beam travelling through the microscope

wavelengths, which will be used to image the sample. The beam then goes through the objective lens and gets focused on the sample we prepared (see Section 2.5) as shown in

Figure 2.3. The most commonly used objective lenses are the $4\times$ objective and the $40\times$ oil objective, which we will discuss further in Section 2.5. A picture of the complete DLW setup is taken and shown below in Figure 2.4.

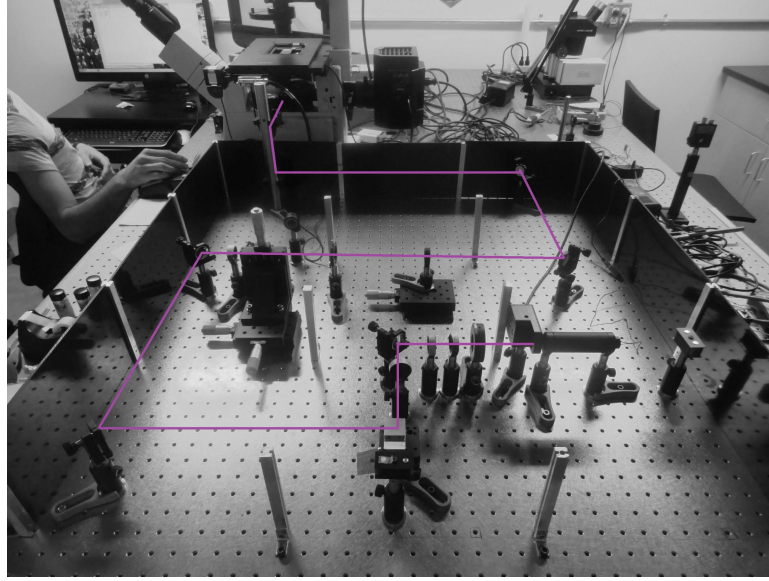


Figure 2.4: Direct Laser Writing Setup (Photo credit: Olja Simoska)

The sample is fixed on an automated stage, which moves in the plane perpendicular to the principle axis of the laser beam. When the laser beam is turned on, polymerization of the photoresist occurs at the spot of exposure. If the automated stage is moving at the same time, a trace of polymerized photoresist shows up on the path in which the focal point of the laser beam moves relative to the sample. A series of planar structures can be fabricated by pre-programming the moves of the stage with a graphical user interface, which will be further discussed in Section 2.5.

2.3 Photoresist

The photoresists that we used throughout the experiments consists of an acrylic ester (monomer), a photoinitiator, and an inhibitor. As described in Sections 1.2, 1.3, and 1.5, the photoinitiator absorbs photonic energy from the laser and turns into radicals. The radicals propagate to form polymer chains as they react with the carbon-carbon double bonds in the acrylate groups. The inhibitor in the photoresist prevents “over-polymerization” by quenching the excessive free radicals generated by photoinitiation.

2.3.1 Composition

The structures of the three components of the photoresist are shown in Figure 2.5. The majority ($\geq 95\%$) of the photoresist is composed of the acrylate monomer, which, in our experiments, is dipentaerythritol-pentaacrylate (SR-399) (Sartomer, USA). The photo-initiator used is Lucirin[®] TPO-L (BASF, Germany). We control the concentration of the photo-initiator to be 1%. Trial experiments have shown that this concentration works the best for a wide ranges of exposure dose, as well as both our objective lenses. Dif-

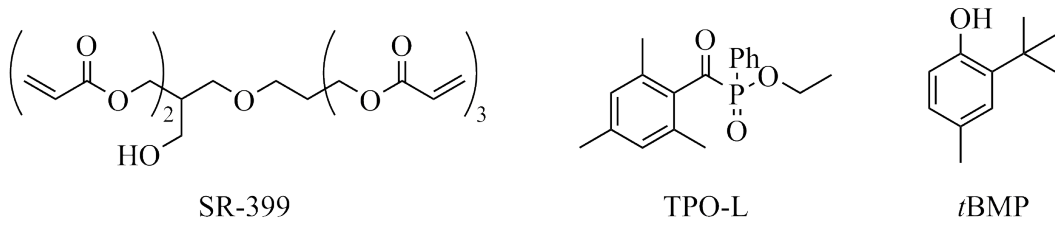


Figure 2.5: Photoresist Composition

ferent concentrations ($0 \sim 4\%$) of radical scavenger 2-*tert*-butyl-4-methylphenol (*t*BMP) (Sigma-Aldrich, USA) were also added into the photoresist as the inhibitor.

2.3.2 Preparation

Four types of photoresists with different concentrations of *t*BMP are prepared according to the mass percentage listed in Table 2.1. Notice that the most significant difference among them is the concentration of *t*BMP. In later experiments, we will investigate the effects of inhibitor on different properties in DLW.

Photoresist #	SR-399	Lucirin® TPO-L	<i>t</i> BMP
1	99%	1%	0%
2	97%	1%	2%
3	96%	1%	3%
4	95%	1%	4%

Table 2.1: Composition (Mass Percent) of Different Photoresists

Because the photo-initiator is photo-sensitive, the preparation of each photoresist is carried out in a dark room. A light-insulating bottle is made by covering the surface of a 20-mL glass vial with aluminum foil as the container for the photoresist. After all compounds are weighed properly and added into the bottle, the mixture is heated to $80 \sim 90^\circ\text{C}$. By reaching this temperature range, *t*BMP melts in the mixture, and the viscosity of the mixture is reduced dramatically for better mixing. At this time, a wooden

applicator is used to mix the components. The photoresist is then cooled in a hood and is ready for use after it gets back to room temperature.

2.4 Modified Glass Slides or Coverslips

Glass is made from silicate salts, and silicate is usually not a good substrate for microfabrication because of its low affinity for acrylate polymers. However, if we perform a modification on the glass surface, the acrylate polymer will attach covalently to the glass surface, resulting in permanent structures on the glass.

Clean, dry glass slides or coverslips (1 in \times 1 in) are cleaned in an air plasma (Harrick Scientific model PDC-32G) for 5 minutes, and then placed in a solution containing 2% (3-acryloxypropyl)-trimethoxysilane (Gelest, USA), 3% water, and 95% ethanol (Sigma Aldrich, USA) for 6 hours with constant stirring. The acrylate-modified coverslips are then rinsed with ethanol twice, dried with nitrogen gas, and heated in an oven at 100°C for 20 minutes. At this point, the surface of the glass slides or coverslips is covered with a layer of acrylate groups. When polymers form under laser exposures, the polymer chains bond to the acrylate groups, leaving tightly bonded structures on the glass surface.

2.5 Constructing a Micro-Scale Structure

A sample for DLW is prepared by placing a drop of photoresist between a clean, dry microscope slide (3 in \times 1 in) and an acrylate modified glass surface. Depending on the

structure we desire to construct, we may use a modified glass slide or coverslip. The difference between these two types of substrates and fabrication techniques are discussed in the following subsections.

2.5.1 Fabrication using the $4\times$ objective lens ($\text{NA} = 0.10$)

Both modified glass slides and coverslips work for this setup. The sample for DLW is fixed on the automated stage above the objective lens. The automated stage, together with the shutter in front of the laser diode, is controlled by a program (ProScan GUI, Miles Ingram) on a computer. Desired structures can be programmed and fabricated automatically with the program. The moving speed of the photonic exposure can be programmed as the moving speed of the automated stage. The power output of the laser diode can be controlled with the half-wave plate and the polarizing beam splitter (Section 2.1). An effective power for DLW with $4\times$ objective lens ranges from $1\ \mu\text{W}$ to $500\ \mu\text{W}$, depending on the fabrication speed.

2.5.2 Fabrication using the $40\times$ oil objective lens ($\text{NA} = 1.30$)

Only modified coverslips work for this setup. Before one starts to fabricate any structure with the $40\times$ objective lens, a drop of index matched immersion oil must be applied to the objective lens. The oil drop then comes into contact with both the lens and the sample on the side of the coverslip. A glass slide cannot be used with this objective because the focal distance of the objective lens is smaller than the thickness of the glass

slide. Structures with much small dimension can be fabricated with the same program as the one we used for $4\times$ objective lens. An effective power for DLW with $40\times$ oil objective lens ranges from 50 nW to 300 nW, depending on both the fabrication speed and the complexity of the structure.

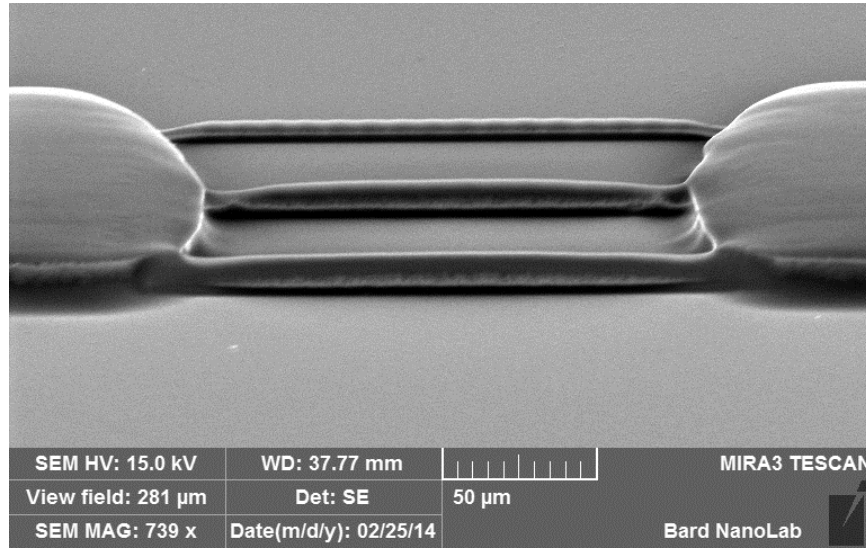


Figure 2.6: A hybrid structure using both objectives

Hybrid structures can be fabricated by combining the advantages of both lenses. A typical size for DLW with the $4\times$ objective is $50 \sim 100 \mu\text{m}$, while that with the $40\times$ oil objective is $1 \sim 3 \mu\text{m}$. The general shape of a structure can be first constructed with the $4\times$ objective, and then the delicate details may be added with the $40\times$ oil objective. An electron micrograph of a successful example is shown in Figure 2.6.

2.6 Developing a Micro-Scale Structure

After the desired structure is successfully fabricated with the pre-programmed commands, the DLW sample is removed from the automated stage. If it just underwent $40\times$ fabrication, the index matched immersion oil should be wiped off the coverslip with hexanes. The sample is then submerged in ethanol for 10 minutes to dissolve the unpolymerized photoresist. The substrate is carefully separated with the microscope slide, and is further rinsed by ethanol and methanol. After drying the DLW sample with gentle flow of air, the structure is ready to be used for further steps including scanning electron microscopy (SEM) imaging, microfluidics, and soft lithography.

2.7 Scanning Electron Microscopy (SEM)

Before sending the fabricated sample to the SEM, a 20-nm layer of gold is sputter coated (Cressington, Model 108 Sputter Coater) to the surface of the sample so that the surface becomes electrically conductive. The sample is then imaged and measured using a field emission scanning electron microscope (Tescan MIRA 3).

Chapter 3

Shrinkage Study

We notice that the acrylate polymer shrinks in size during the alcohol-rinsing process.

Such shrinkage may affect the accuracy in further studies on memory effect. We also notice that the shrinkage of the polymer depends on the concentration of the inhibitor.

As shown in Figure 3.1, the polymer created with the inhibitor-containing photoresist exhibits more significant shrinkage than the other. Here we present a set of methods to quantitatively characterize the shrinkage of the acrylate polymer.

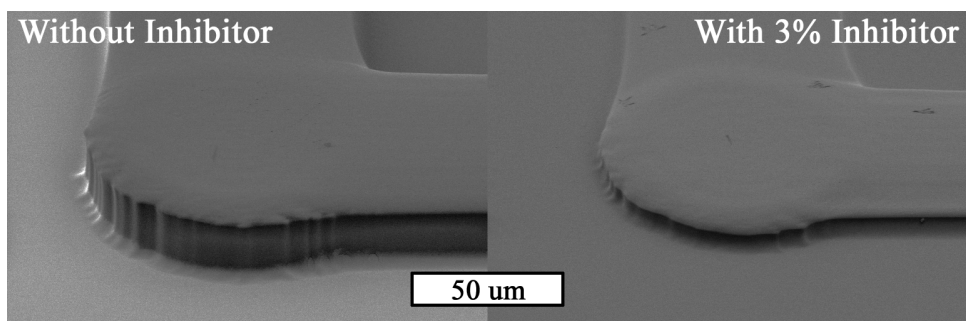


Figure 3.1: Comparison between the shrinkage of two photoresists

3.1 Methods

A sample for DLW was prepared as described in Section 2.5. With the $4\times$ objective lens, a set of lines with different linewidths ranging from $50\ \mu\text{m}$ to $200\ \mu\text{m}$ was fabricated ($100\ \mu\text{W}$, $500\ \mu\text{m/s}$) on the modified coverslip. The linewidths of the lines were first measured under the optical microscope before rinsing. After the first round of measurements, the sample was rinsed with alcohols and dried over blowing nitrogen gas. It is then sputter-coated and sent to the SEM for measurements after alcohol developing. Two sets of measurements were tabulated and compared to obtain the shrinkage coefficient for the photoresist. The process was repeated with four different photoresists.

Near the surface of the modified coverslip, the shrinkage behavior is restricted because the polymer chains are bonded to the acrylate groups on the surface of glass. We introduce a new method to characterize the shrinkage coefficients of the photoresists. The data obtained by this method are of more interest to this project because most of the following experiments are carried out with $40\times$ oil lens, and so is this method.

A sample for DLW was prepared as described in Section 2.5. With the $40\times$ oil objective lens, four columns of dimension $10\times 10\times 10\ \mu\text{m}$ were fabricated ($80\ \text{nW}$, $50\ \mu\text{m/s}$) layer by layer with different focal depth. The columns were then connected with two single-pass DLW at $10\ \mu\text{m}$ above the surface of coverslip, forming a cross in the middle of the structure. A 10-by-10- μm grid of lines was subsequently drawn on the cross to yield a waffle-like structure floating in the center. A 3-D presentation of the structure is shown

in Figure 3.2. The sample was then rinsed with alcohols and dried carefully by letting the alcohols evaporate. As the alcohols evaporated away, the waffle structure was pulled onto the surface of the glass due to surface tension of the remaining fluid. After the sample was completely dried, it was sent for sputter-coating and SEM imaging to determine the dimension of the waffle structure after alcohol developing.

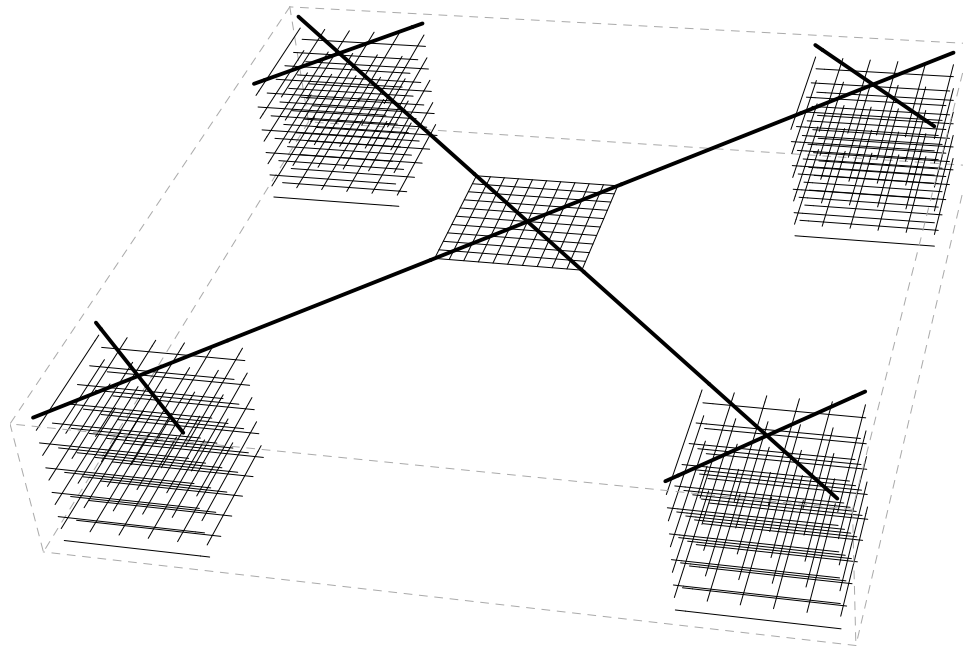


Figure 3.2: Structure Used to Measure the Shrinkage Coefficient

3.2 Results

The results are generally consistent with our conjecture. We present the results from different methods in two separate subsections.

3.2.1 Shrinkage with the $4\times$ objective lens

The measured linewidths before and after alcohol developing are tabulated in Table A.1 – A.4 in Appendix A. For each photoresist, we plot the linewidth before developing *v.s.* the linewidth after (Figure A.1 – A.4). The slope of the plot indicates the proportion of remaining linewidth, which can be used to calculate percent shrinkage of each photoresist (Table 3.1).

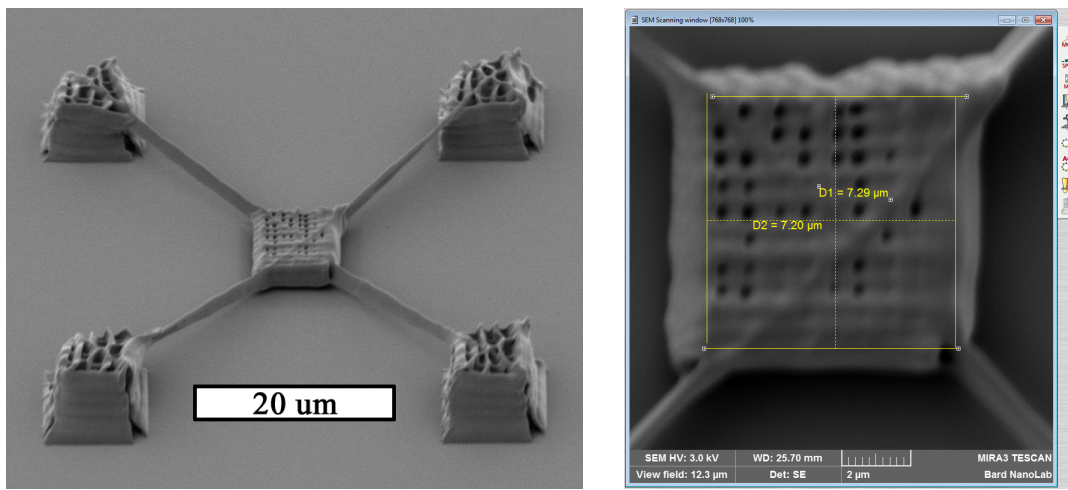
Photoresist #	Regression Formula	% Remaining	% Shrinkage
1	$y = 0.870413x$	87%	13%
2	$y = 0.876853x$	88%	12%
3	$y = 0.856793x$	86%	14%
4	$y = 0.803336x$	80%	20%

Table 3.1: Percent Shrinkage of Each Photoresist

3.2.2 Shrinkage with the $40\times$ oil objective lens

The highly concentrated exposure dose for fabricating the structure illustrated in Figure 3.3a gave rise to troubles in measuring the actual dimension of the waffle structure because the central structure had increased in size due to memory effect (Section 1.4). Fortunately, the polymer retained its waffle-like texture so that we were able to measure the distance between the first and the last swells of the structure in both *x* and *y* direc-

Figure 3.3. The results are tabulated in Table 3.2.



(a) Waffle Structure at 45° of View (b) Measuring the waffle structure

Figure 3.3: Waffle Structure and Measuring Scheme

Photoresist #	Original Size	After Developing		% Shrinkage
		<i>x</i> -direction	<i>y</i> -direction	
1	10 μm	8.04 μm	8.04 μm	20%
2	10 μm	7.67 μm	7.91 μm	22%
3	10 μm	7.37 μm	7.61 μm	25%
4	10 μm	7.20 μm	7.29 μm	28%

Table 3.2: Shrinkage Coefficients of Photoresists under 40 \times Oil Condition

3.3 Discussion

The measurements with both $4\times$ and $40\times$ objective lenses showed that the percent shrinkage increases as the concentration of inhibitor in the photoresist increases. This conclusion explained the different appearance of polymers under the same fabricating conditions with different photoresists (Figure 3.1).

The results obtained from the $4\times$ air objective lens appeared to be more controversial. The percent shrinkage of the first three photoresists are close in range (12% - 14%). However, there were more systematic errors involved in this method: (1) the shrinking restriction and (2) the power dependence.

The polymers fabricated with $4\times$ lens bond to the surface of the glass, preventing it from shrinking near the base. In the $40\times$ case, the polymers to be measured were fabricated without contacting the surface of the glass, and thus able to shrink evenly in all directions.

The present shrinkage also appeared to be power-dependent in the $4\times$ case. For instance, the separated branches in the plot for photoresist #1 (Figure A.1) were the outcome of changing the laser power (from $10\ \mu\text{W}$ to $100\ \mu\text{W}$) during the experiment. However, the percent shrinkage is less power-dependent in the $40\times$ case because the useful power range for $40\times$ oil fabrication ($50\ \text{nW} \sim 300\ \text{nW}$, see Chapter 4) is much narrower than that for $4\times$ fabrication.

Chapter 4

Linewidth Characterization

One of the most fundamental and most useful structure for DLW lithography is a straight line. In this chapter, we present a study on the properties of straight lines fabricated from DLW under different conditions. We used different laser powers, writing speeds, and inhibitor concentrations, and compared the linewidths under these conditions. The results gives a table of reference for future fabrication of lines with desired linewidth.

4.1 Methods

A sample for DLW was prepared as described in Section 2.5. A straight line was first drawn on the coverslip while adjusting the z -coordinate in order to align the focal point of the laser with the surface of the coverslip. A set of five straight lines with a specific power-speed combination was drawn $100 \mu\text{m}$ away from the focus-adjustment line

in order to prevent significant memory effects. The sample was developed and sputter-coated, then sent for SEM imaging as described in Sections 2.6 and 2.7. An SEM image of the fabricated straight lines is shown in Figure 4.1. Such process was repeated for all the power-speed combinations for the following choices of laser powers and writing speeds in Table 4.1. The measured linewidth under each condition is tabulated and compared for the analysis of the linewidth's dependence on different conditions.

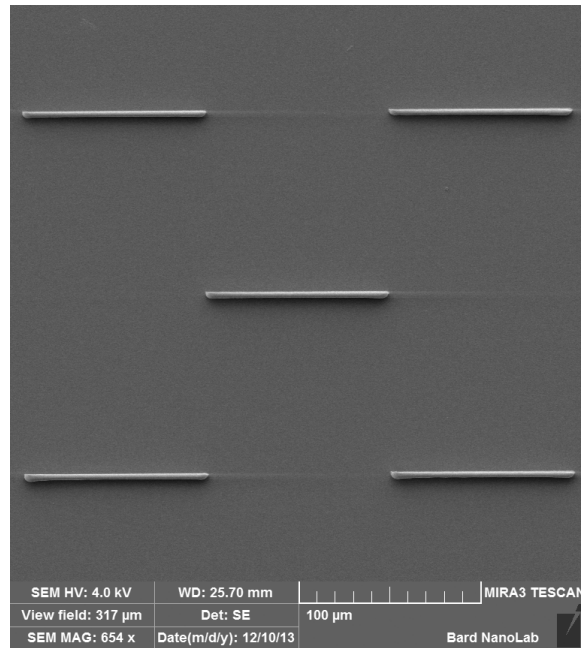


Figure 4.1: Straight Lines for Linewidth Measurements

Laser Power (nW)	100	150	200	250
Writing Speed ($\mu\text{m}/\text{s}$)	20	30	40	50

Table 4.1: Laser Powers and Writing Speeds for Linewidth Characterization

In order to reduce the unexpected variations during the fabrication, and to save the usage of modified coverslips, all the sixteen combinations were operated on one sample. Then the same combinations were repeated for the other photoresists. In the end, we obtained a total of 64 sets of lines for linewidth measurements.

4.2 Results

The raw data of linewidth measurements on the 64 sets of lines are tabulated in Appendix B. The “not available” (N/A) data points are conditions under which linear fabrication was difficult, if not impossible, due to low laser power and/or high writing speed. The average linewidths obtained from different fabricating conditions are tabulated in Table B.5. A more viewer-friendly colored chart is also provided as Figure 4.2 on the following page with the numbers showing the linewidths under the according fabricating conditions.

4.3 Discussion

The colored chart provides a clear pattern within the data. The linewidth of DLW depends on laser power, writing speed, and inhibitor concentration in the photoresist. In all four photoresists, the color of the blocks turns “colder” as we go down the rows for higher laser power, and turns “warmer” as we go right of the columns for faster writing speed. As we increase the inhibitor concentration, the color of the chart turns “warmer”.

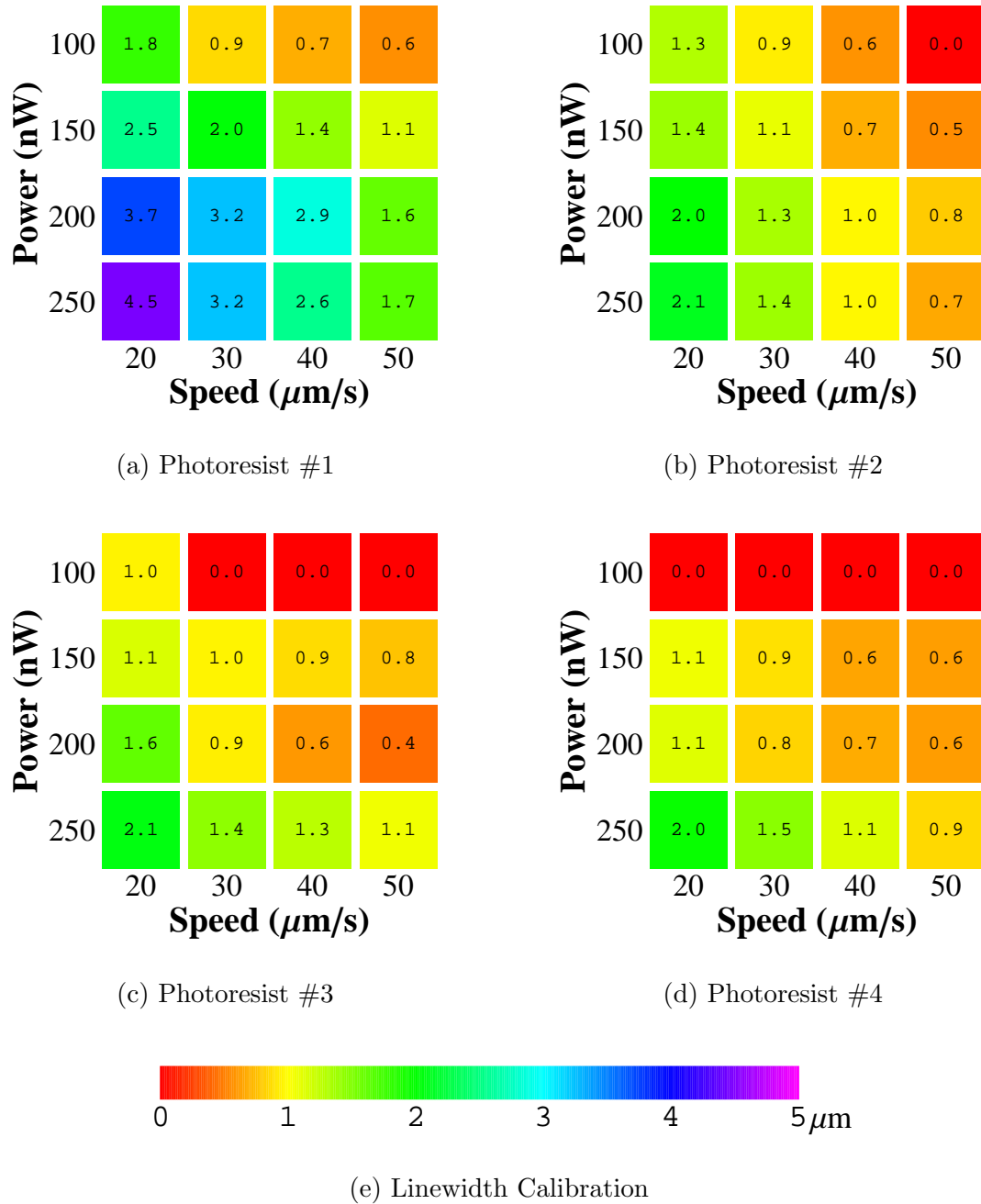


Figure 4.2: Linewidths under Different Conditions

The colored chart provides a table of reference for future fabrications of lines with desired linewidth.

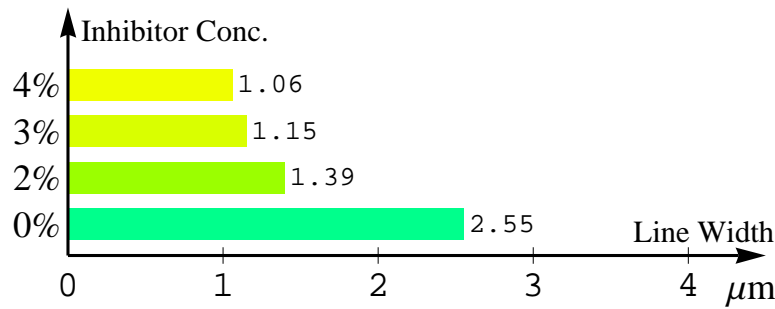
4.3.1 Laser power/writing speed dependence

Generally in the colored chart, as we go down each row, the color of the blocks turns “colder”, and the linewidth increases. It makes sense that thicker lines are fabricated with higher laser power.

All the rows in the colored chart have linewidth value decreasing from left to right. Thus the linewidth decreases as we increase the writing speed, because the exposure dose is reduced in a unit area with a faster speed.

4.3.2 Inhibitor concentration dependence

The general picture shows that the color of the charts turns “warmer” as the concentration of inhibitor is increased. Here we compare the linewidths under one power-speed combination for four different photoresists to illustrate the inhibitor’s affects on DLW linewidth. Figure 4.3 shows the average linewidths of straight lines fabricated under 150 nW laser power and 20 $\mu\text{m}/\text{s}$ writing speed with four different photoresists. As we may tell from the figure, the average linewidth measured from the SEM image decreases with an increasing inhibitor concentration. However, we are more interested in the linewidths before shrinkage, which can be calculated with the shrinkage coefficient determined in Section 3.2. The linewidth before shrinkage for each photoresist is tabulated in Table 4.2,

Figure 4.3: Linewidths under 150 nW, 20 $\mu\text{m}/\text{s}$ with different photoresists

Photoresist	Measured linewidth	% Shrinkage	Calculated linewidth
#1	2.55 μm	20%	3.19 μm
#2	1.39 μm	22%	1.78 μm
#3	1.15 μm	25%	1.53 μm
#4	1.06 μm	28%	1.47 μm

Table 4.2: Calculated linewidth from shrinkage coefficients

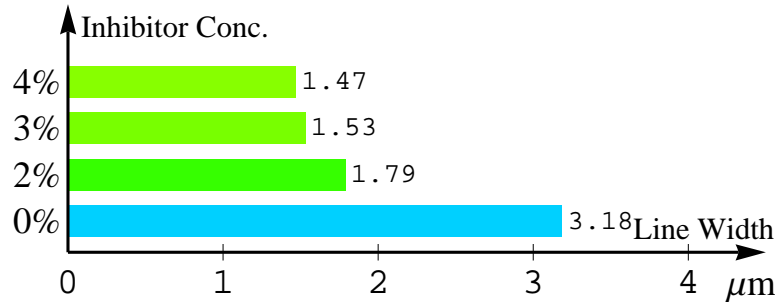


Figure 4.4: Calculated linewidths with different photoresists

and plotted in Figure 4.4. We arrive at the same conclusion that the average linewidth decreases with an increasing inhibitor concentration.

Part II

Mathematical Modeling

Chapter 5

Introduction II

One of the most important concerns in the area of direct laser writing (DLW) lithography is the spatial resolution. However, the spatial resolution of DLW lithography is affected by the memory effect. The diffusive behavior of the photoresist prohibits structures from being fabricated close to each other. The *heat equation*, which is classified as a *parabolic partial differential equation*, describes the heat flow or diffusion processes. A simple example of the heat equation in one-dimension is given by

$$\frac{\partial}{\partial t}u(x,t) = \alpha \cdot \frac{\partial^2}{\partial x^2}u(x,t), \quad (5.1)$$

where $u(x,t)$ is a function of space x and time t that describes the concentration of a specific molecule in a heterogeneous mixture, where $\alpha > 0$ is the diffusivity coefficient. Previous research showed the utility of heat equations in this type of modeling [PY05]. We assume that the diffusion of the particles, including the monomer, photoinitiator, and

free radicals, behave according to an analog of the heat equation. Therefore, it is natural to start with the heat equation and develop a mathematical model for the polymerization of the photoresist.

However, a PDE does not always have analytic solutions [Rub74]. In order to obtain numerical approximations of the solutions to PDEs, the *method of finite differences* is used to discretize the continuous partial differential equations into difference equations. The difference equations can then be iteratively solved with appropriate initial and boundary conditions with the help of mathematical programming languages.

Additionally, we use *Markov chains* to model the growth of the polymer. Similar approach had been applied in the modeling of actin polymerization [Sza10]. A Markov chain is a deterministic probabilistic model with a finite number of *states* $\{s_i\}_{i=1}^n$ and transition probabilities $\{p_{ij} \mid 1 \leq i, j \leq n\}$ between states s_i and s_j . The Markov process assumes that the conditional probability distribution of future states of the process depends only upon the present state, not on the sequence of events that preceded it. The Markov model gives a probabilistic distribution of states at any given number of time steps [Rev84].

5.1 The Gaussian Beam

Before we start modeling the polymerization reaction, we study the profile of the laser setup. In Section 2.1, we proposed that the intensity of the collimated laser beam follows

the pattern of an Airy disk, which can be approximated by a Gaussian function. The beam can therefore be approximated as a Gaussian beam (Section 2.1 and Figure 2.2). We shall present some useful properties of the Gaussian beam [ST91].

The *optical intensity* of a focused Gaussian beam $I(\mathbf{r})$ is a function of the axial and radial distances, z and $\rho = \sqrt{x^2 + y^2}$, respectively. The expression is given by

$$I(\rho, z) = I_0 \left[\frac{W_0}{W(z)} \right]^2 \text{Exp} \left[-\frac{2\rho^2}{W(z)^2} \right], \quad (5.2)$$

where I_0 is the intensity at the center of the beam, W_0 is the *beam waist*, and $W(z)$ is the *beam radius* at z , given by

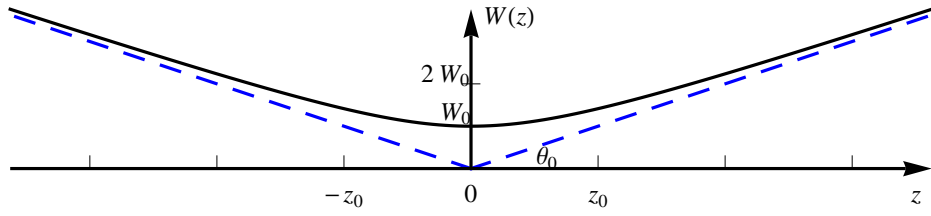
$$W(z) = W_0 \sqrt{1 + \left(\frac{z}{z_0} \right)^2}, \quad (5.3)$$

where z_0 is called the *Raleigh range*, and is the axial distance at which the intensity is half of I_0 along the beam axis.

Two additional properties of the Gaussian beam used in developing the model are the *beam divergence* and the *depth of focus*. Far from the beam center, when $z \gg z_0$, the beam radius increases approximately linearly. This fact can be verified by examining the beam radius function $W(z)$. By algebraic manipulation, we may get the relation

$$\frac{W(z)^2}{W_0^2} - \frac{z^2}{z_0^2} = 1, \quad (5.4)$$

which implies that $W(z)$ is the positive branch of a pair of hyperbolae. The plot of $W(z)$, therefore, has a pair of linear asymptotes (Figure 5.1), which defines a half-angle. About 86% of the beam power is confined with a cone defined by the half-angle θ_0 [ST91]. The

Figure 5.1: Beam Radius as a Function of z

angular divergence of the beam is therefore defined by the angle

$$\theta_0 = \frac{2}{\pi} \cdot \frac{\lambda}{2W_0}. \quad (5.5)$$

The beam divergence is inversely proportional to the beam-waist diameter $2W_0$. Thus if we want to squeeze the beam waist to produce a smaller DLW voxel, a larger θ_0 should be used by using a lens with high numerical aperture (NA).

The Gaussian beam achieves its best focus at the plane $z = 0$. In either direction, the beam gradually grows “out of focus.” The axial distance within which the beam radius lies within a factor of $\sqrt{2}$ of its minimum value is known as the *depth of focus* or *confocal parameter*, and is twice the Rayleigh range,

$$2z_0 = \frac{2\pi W_0^2}{\lambda}. \quad (5.6)$$

In our $40\times$ oil setup (See Section 2.5), we know the numerical aperture (NA) of the objective lens and the refractive index n of the index matched immersion oil. Thus we compute the angular divergence of the Gaussian beam

$$\theta_0 = \sin^{-1} \left(\frac{\text{NA}}{n} \right). \quad (5.7)$$

With the help of the angular divergence formula (5.5), we may figure out the beam waist

$$W_0 = \frac{\lambda}{\pi\theta_0} = \frac{\lambda}{\pi \sin^{-1}(\text{NA}/n)} \quad (5.8)$$

Now we substitute the numerical values $\lambda = 0.405 \mu\text{m}$, $\text{NA} = 1.3$, and $n = 1.5$ in, and obtain the beam waist $W_0 = 0.123 \mu\text{m}$. Thus the intensity function (5.2) at $z = 0$ is

$$I(r, \theta) = I_0 \cdot \text{Exp}\left(-\frac{2r^2}{W_0^2}\right), \text{ where } W_0 = 0.123 \mu\text{m}. \quad (5.9)$$

We integrate the intensity function over the whole plane in polar coordinates to get the power output of the Gaussian beam:

$$P = \iint_{\mathbb{R}^2} I(r, \theta) dA = \int_{\theta=0}^{2\pi} \int_{r=0}^{\infty} I_0 \cdot \text{Exp}\left(-\frac{2r^2}{W_0^2}\right) \cdot r dr d\theta = \frac{\pi I_0 W_0^2}{2}. \quad (5.10)$$

Therefore, once we measure the power output P of the approximated Gaussian beam after the pinhole, we may use the equation

$$I_0 = \frac{2P}{\pi W_0^2} \quad (5.11)$$

to compute the principal intensity. Thus we have the complete Gaussian beam profile, with the radial distance r and axial distance z from the center of exposure as the only two dependent variables.

5.2 Parabolic Equations

To describe diffusive behaviors of particles, we need parabolic-type partial differential equations. First we shall have some definitions [Far82].

Definition 1. A *partial differential equation*, abbreviated as **PDE**, is an equation that contains partial derivatives.

Let $u(x, y)$ be a function of x and y . Listed below are some examples of partial differential equations.

$$\frac{\partial u}{\partial x} = 0, \quad \frac{\partial^2 u}{\partial x^2} + \frac{\partial^2 u}{\partial y^2} = 0, \quad u^2 + \frac{\partial u}{\partial x} = f(x, y).$$

For notational simplicity, we would denote the partial derivatives using subscripts as follows

$$u_x = \frac{\partial u}{\partial x}, \quad u_y = \frac{\partial u}{\partial y}, \quad u_{xx} = \frac{\partial^2 u}{\partial x^2}, \quad u_{yy} = \frac{\partial^2 u}{\partial y^2}.$$

Definition 2. Let $u(x, y)$ be a function of two variables x and y . A **second-order linear PDE in two variables** is an equation in the form

$$Au_{xx} + Bu_{xy} + Cu_{yy} + Du_x + Eu_y + Fu = G,$$

where A, B, C, D, E, F, G can be constants or given functions of x and y .

Definition 3. **Parabolic equations** are second-order linear PDEs which satisfy the property $B^2 - 4AC = 0$. Parabolic PDEs are often used to describe heat flow and diffusion processes.

Definition 4. The **one-dimensional heat equation** is a PDE in the form

$$u_t = \alpha \cdot u_{xx},$$

where u is a function of space x and time t , and $\alpha > 0$ is the diffusivity coefficient.

The heat equation is parabolic because $0^2 - 4\alpha \cdot 0 = 0$, and it is capable of describing the diffusion of particles in a system. However, the heat equation only describes linear diffusive behaviors under conservative conditions. The introduction of *source* and *sink* terms enables us to incorporate the non-conservative behaviors of concentrations. Notice that the left-hand side of the heat equation is the partial derivative of the concentration function with respect to time, in other words, the rate of change in concentration. A positively-valued term added to the right-hand side leads to the increase in u_t , and we name such term a *source*. On the other hand, a negatively-valued term is named a *sink*. These terms describes the non-conservative increase or decrease in concentrations of species in the system.

In addition, to solve differential equations, we need *initial conditions* and *boundary conditions*. The initial condition provides information about the concentration in the system at an initial time. The boundary conditions are given to compensate for the fact that the partial derivatives are not well-defined at the boundaries. During the diffusion process, there should be no net flow of particles through the boundary, *i.e.*, the spatial derivatives at the boundaries should be zero. This type of boundary conditions is called *Neumann boundary conditions*.

With an appropriate system of parabolic PDEs, initial, and boundary conditions, we shall proceed to numerically solve the system with the method of finite differences, since it would be too hard, if not impossible, to solve analytically.

5.3 Method of Finite Differences

The differential equations with sink and source terms described in the previous section are usually nonlinear, and thus too complicated to be solved analytically. We need to devise our toolbox with numerical methods to solve them. Of the many different approaches to solving PDEs numerically, we use the *method of finite differences* to numerically approximate our physical reality [Tho95]. The method of finite differences converts differential equations to *difference equations*, whose spatial and time domains are discrete. There are yet other numerical methods that are more efficient and accurate, but the method of finite differences is easier to implement in a programming language. We use Wolfram Mathematica® to numerically solve the PDEs which simulate the physical problem.

To start, we consider the initial-boundary-value problem of heat flow. Let $V(x, t)$ be a function of temperature in terms of space x and time t on the domain $x \in [0, 1]$. Let $f(x)$ be a function defined on $x \in [0, 1]$, and let $a(t)$ and $b(t)$ be functions defined on $t \in [0, \infty)$. Suppose that $V(x, t)$ satisfies

$$V_t = \alpha \cdot V_{xx}, \quad x \in (0, 1), \quad t > 0 \quad (5.12)$$

$$V(x, 0) = f(x), \quad x \in [0, 1] \quad (5.13)$$

$$V(0, t) = a(t), \quad V(1, t) = b(t), \quad t \geq 0 \quad (5.14)$$

where the initial condition and the boundary conditions agree, *i.e.*, $f(0) = a(0)$ and $f(1) = b(0)$. Our first step is to convert the continuous system into a discrete expression. We discretize the spatial domain into $M + 1$ equally spaced points $x_0, x_1, \dots, x_{M-1}, x_M$,

where $x_0 = 0$, $x_M = 1$, and $x_k = k\Delta x$ for all integer-valued k that satisfies $0 \leq k \leq M$ and $\Delta x = 1/M$. Likewise, we discretize the time domain with spacing Δt , and we have points t_0, t_1, \dots on the time domain, where $t_n = n\Delta t$ for all integer-valued $n \geq 0$. Hence, we obtain a *grid* on the space-time domain as shown in Figure 5.2.

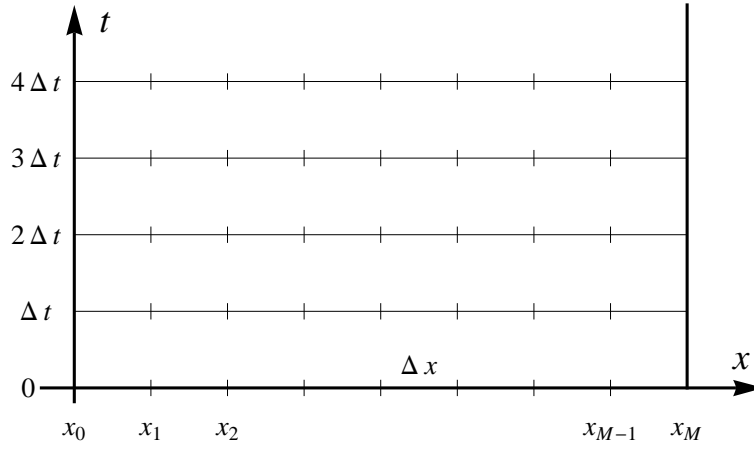


Figure 5.2: Difference Grid on the Space-Time Domain

The lattice points in the figure approximate the system (5.12)–(5.14) as $\Delta x \rightarrow 0$ and $\Delta t \rightarrow 0$, and we shall define $v(k, n)$ to be a function defined at the point $(k\Delta x, n\Delta t)$, in which case v approximates V . By definition of a derivative, we know that

$$V_t(x, t) = \lim_{\Delta t \rightarrow 0} \frac{V(x, t + \Delta t) - V(x, t)}{\Delta t}. \quad (5.15)$$

Thus it is reasonable to define the *derivative* of the discrete function $v(k, n)$ by

$$v_t(k, n) = \frac{v(k, n + 1) - v(k, n)}{\Delta t}. \quad (5.16)$$

Likewise, the second spatial derivative of $v(k, n)$ may be defined by the centered difference

equation

$$v_{xx}(k, n) = \frac{v(k+1, n) - 2v(k, n) + v(k-1, n)}{\Delta x^2}. \quad (5.17)$$

Thus the approximated differential equation (5.12) is written as

$$\frac{v(k, n+1) - v(k, n)}{\Delta t} = \alpha \cdot \frac{v(k+1, n) - 2v(k, n) + v(k-1, n)}{\Delta x^2}, \quad (5.18)$$

or, equivalently,

$$v(k, n+1) = v(k, n) + \alpha \cdot \frac{\Delta t}{\Delta x^2} \cdot \left(v(k+1, n) - 2v(k, n) + v(k-1, n) \right), \quad (5.19)$$

and the initial condition and the boundary conditions are approximated by

$$v(k, 0) = f(k\Delta x) \quad (5.20)$$

$$v(0, n+1) = a((n+1)\Delta t) \quad (5.21)$$

$$v(M, n+1) = b((n+1)\Delta t) \quad (5.22)$$

The equations (5.19)–(5.22) provide an approximation for the system (5.12)–(5.14). Because we already know the initial values of v at all lattice points and the boundary values of v at all time from equations (5.20)–(5.22), we may use equation (5.19) to iteratively compute the value of v at each lattice point, thus giving a discrete numerical approximation for the continuous function $V(x, t)$.

5.4 Markov Chains

A probabilistic model for the acrylate polymerization can be presented as a directional *random walk* [Sza10]. A random walk is a random process consisting of a sequence of

discrete steps. Consider a particle on the number line with initial location $x = 0$. In a directional random walk, there are two and only two possible options for the particle in a time unit: there is a probability p that the particle jumps one unit to the right, and a probability q that it stays at its current location. Additionally, the probabilities must sum to one, *i.e.*, $p + q = 1$. The *states* (position of the particle) and the *transition probabilities* between states together form a *Markov chain* as shown by the *state diagram* in Figure 5.3. The Markov chain satisfies the *Markov assumption* that the probability of transition is only dependent on the current state and independent from all previous ones, thus can be modeled as a Markov process.

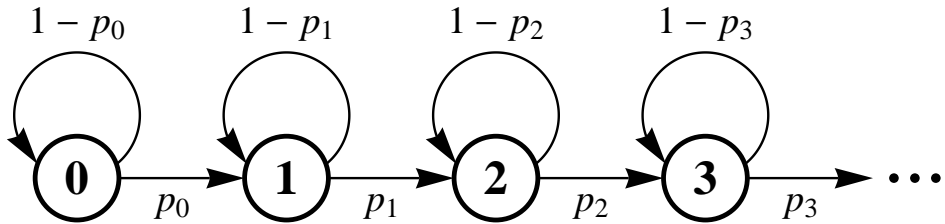


Figure 5.3: A State Diagram of the Markov Chain for Directional Random Walk

Define $P(k, t)$ for all $k \in \mathbb{N}$ and $t \in \mathbb{N}$ as the probability of the particle being at position k at time t , and let p_k be the transition probability for a transition from k to $k + 1$ for all $k \in \mathbb{N}$. Given an initial probability density function $P(k, 0)$ of where the particle might be, the probability density $P(k, i + 1)$ at the $(i + 1)$ -th time step can be given by

$$P(k, i + 1) = P(k, i) \cdot (1 - p_k) + P(k - 1, i) \cdot p_{k-1}. \quad (5.23)$$

The first term on the right hand side stands for the probability that the particle was at

position k at the i -th time step, and did not move in the subsequent time iteration; the second term stands for the probability that the particle was at position $k - 1$ at the i -th time step, and moved one step forward in the subsequent time iteration. Mathematical induction allows us to iteratively approximate the probability density $P(k, t)$ at the t -th time step for all $k \in \mathbb{N}$. The *expected value* $E[K, t]$ of the location of the particle at time t can be computed with

$$E[K, t] = \sum_{k=0}^{\infty} k \cdot P(k, t). \quad (5.24)$$

We may use this expected value as the expected position of the particle at time t .

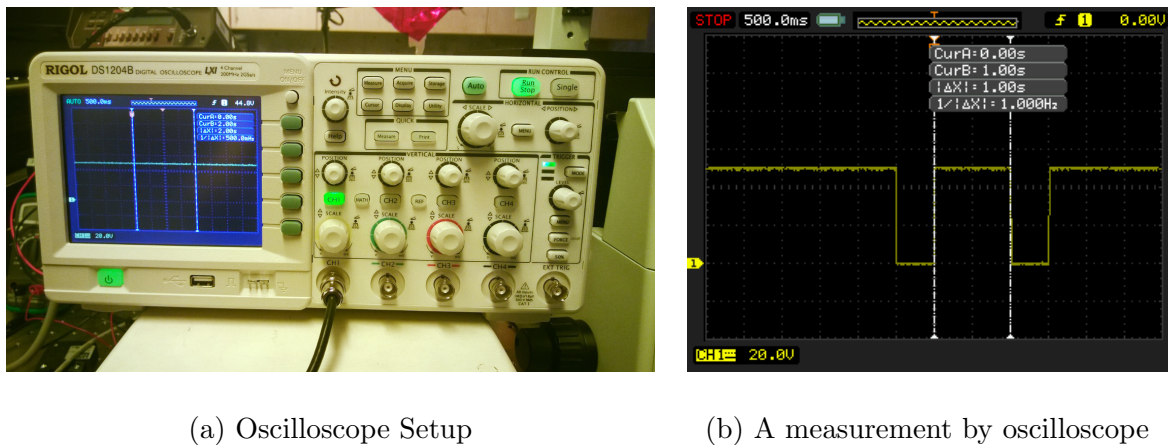
Chapter 6

Memory Effect Characterization

The ultimate goal of this project is to develop a mathematical model that describes the acrylate polymerization reaction as well as the memory effect (Section 1.4). Here we present an experimental method to quantify the memory effect. We studied the simplest case – two dots drawn consecutively with a *hiatus* time in between. Because both the diffusive behavior and the decay of radicals depend heavily on time, we need to accurately measure all the time periods between and during events. In addition to our usual setup, we used an oscilloscope to measure the exposure time and hiatus time. The percent growth in dot size is measured and tabulated for different spacing and hiatus time conditions, and is used as a measure of the “extent” of memory effect.

6.1 Oscilloscope Setup

A digital oscilloscope (Rigor DS1204B) was connected to the shutter control to monitor the electronic signals. The voltage output of the shutter trigger was connected to Channel 1 of the oscilloscope. The time scale was set to be 500.0 ms per grid, and the voltage scale was set to be 20.0 V per grid (Figure 6.1a). For monitoring a double-dot exposure, the oscilloscope run control was set to “Single”, which is triggered by a change in the input voltage. A measurement of 0.50-second exposure time and 1.0-second hiatus time is shown in Figure 6.1b.



(a) Oscilloscope Setup

(b) A measurement by oscilloscope

Figure 6.1: Digital oscilloscope used in the experiment

6.2 Methods

A sample for DLW is prepared as described in Section 2.5. Then pairs of dots with 0.50-second exposure time were fabricated with spacing and hiatus time listed in Table 6.1.

Spacing (μm)	Hiatus time (s)	Base speed range (μm/s)
10.0	2.0	5.7 – 5.9
	1.0	11.5 – 11.7
	0.50	24.3 – 24.6
8.0	2.0	4.8 – 5.0
	1.0	10.2 – 10.5
	0.50	21.8 – 22.1
5.0	2.0	3.1 – 3.3
	1.0	6.3 – 6.6
	0.50	13.8 – 14.1

Table 6.1: Base Speed Range for Specific Hiatus Time

Depending on the amount of index matched immersion oil applied between the sample and the lens, the actual moving speed of the automated stage differs from the base speed set by the DLW program. The base speed of the program was adjusted according to Table 6.1 so that the hiatus time can be as close to the desired value as possible. At the same time, a camera (Thorlabs UC480) mounted on the microscope was set to a resolution of 480×240 pixels with a frame rate of 101.61 frames per second for further high-speed analysis in the model. The laser power was set to 200 nW. When the laser, program, oscilloscope, and camera were all prepared accordingly, a double-dot fabrication was operated with the camera taking a high-speed video. After all the double-dots were

completed, the sample was washed in ethanol and dried with gentle breeze of air. It was then sputter-coated with gold and sent for SEM imaging, where we obtain data for the dot sizes in each double-dot fabrication.

6.3 Results

The size of each dot under each fabrication are listed in Table 6.2. Notice that some of the hiatus times or exposure times were not controlled exactly the same as the desired value because the machine sometimes had unpredictable electronic delays. In addition, the last two sets (#8, #9) of measurements are not provided because the two dots merged with each other due to the lack of space between them. Figure 6.2 shows the outcome of measurement #9. The SEM images of all nine sets of double-dot measurement are provided in Appendix C.

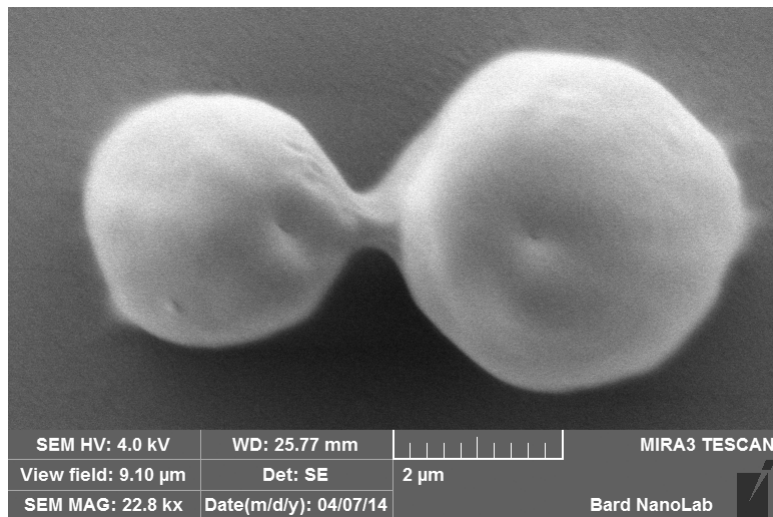


Figure 6.2: SEM Image of Double-Dot Experiment #9

#	Spacing (μm)	1 st exposure (s)	2 nd exposure (s)	Hiatus time (s)	1 st Dot (μm)	2 nd Dot (μm)	% Increase
1	10	0.50	0.50	2.0	1.81	2.09	15%
2	10	0.50	0.50	1.0	2.07	2.56	24%
3	10	0.50	0.50	0.54	1.99	2.63	32%
4	8	0.50	0.50	2.0	1.80	2.14	19%
5	8	0.50	0.50	1.0	2.09	2.70	29%
6	8	0.50	0.56	0.50	2.30	3.37	47%
7	5	0.50	0.54	2.0	2.70	3.28	21%
8	5	0.50	0.56	1.0	—	—	—
9	5	0.50	0.50	0.50	—	—	—

Table 6.2: Dot Size Measurements for Memory Effect

6.4 Discussion

From Table 6.2, two points can be concluded:

- if the spacing between two dots is controlled, the shorter the hiatus time, the larger the percent increase in size;
- if the hiatus time between two dots is controlled, the shorter the distance between them, the larger the percent increase in size.

This result is within our expectation, because the memory effect is conjectured to be a result of excessive amount of radicals and oligomer molecules due to non-local exposure and diffusive behaviors. The diffusion needs time to proceed, thus in a given amount of time, the further away the second exposure is, the less influence from the first exposure imposes on the second. The radicals also decay when two of them quench each other (Section 1.3). The decay process also has a rate, so that the longer we wait after we fabricate the first dot, the less influence from the first exposure imposes on the second.

Chapter 7

Modeling the Memory Effect

We first modeled the memory effect with the heat equation and approximated the changes in the concentration of photoinitiator and radicals (including initial radicals, acrylate monomer radicals, and acrylate oligomer radicals). The PDEs were numerically solved with the method of finite differences, and the solutions were computed in Mathematica as functions of space and time. We then associated the transition probabilities of a Markov chain to the radical concentration, and utilized the Markov chain to generate a probabilistic model that describes the growth of polymer. When the model was completed, the parameters were adjusted so that the results from the model better fit the experimental data obtained in Chapter 6.

In order to prevent confusion, a table of variables and coefficients, and a table of functions and lists, are provided in Tables 7.1 and 7.2.

Variables in Model	Variables in Code	Definitions and Comments
—	ExposureTime1	Variable for the first exposure time in s
—	ExposureTime2	Variable for the second exposure time in s
—	HiatusTime	Variable for the hiatus time in s
—	Spacing	Variable for the spacing between two dots in μm
λ	Lambda	Wavelength of laser in μm , specifically, $\lambda = 0.405$
P	P	Power output of the laser in nW, specifically, $P = 200$
θ	Theta	Angular divergence of the Gaussian beam
z	z	Axial distance from the center of the beam in μm
z_0	z0	Raleigh range in μm
W_0	w0	Beam waist in μm
I_0	I0	Principal intensity of the beam in W/m^2
α	alpha	Diffusivity of photoinitiator
β	beta	Diffusivity of radicals
m	m	Proportion of photoinitiator yield to beam intensity
d	d	Dying coefficient of radicals
M	M	Total number of spatial grids, specifically, $M = 400$
Δx	dx	Length of each spatial step in μm
Δt	dt	Length of each time step in s, specifically, $t = 0.002$
k	k	Index of spatial steps ($0 \leq k \leq M$)
n	n	Index of time steps ($n \geq 0$)

Table 7.1: Table of Variables and Coefficients

Functions in Model	Functions in Code	Definitions and Comments
$W(z)$	<code>W[z]</code>	Returns the beam radius in μm
$I(x)$	<code>Intensity[x]</code>	Returns the beam intensity in W/m^2
$R(x)$	<code>Reflection[x]</code>	Returns the reflection intensity in W/m^2
—	<code>Exposure[x, pos]</code>	Returns the exposure dose given the exposure at <code>pos</code>
p	<code>densityP[u]</code>	Returns the probability of polymerization given the concentration u of radicals
<hr/>		
c	<code>c</code>	List storing the photoinitiator concentration
u	<code>u</code>	List storing the radical concentration
P_l	<code>pLeft</code>	List storing the spatial probability distribution of the left boundary of the polymer
P_r	<code>pRight</code>	List storing the spatial probability distribution of the right boundary of the polymer
—	<code>Poly</code>	List storing the polymerized spatial grids

Table 7.2: Table of Functions and Lists

7.1 First Approximation: Radical Initiation

The first chemical change we approximate is the consumption of the photoinitiator. The concentration of the photoinitiator is denoted $c(x, t)$ as a function of space x and time t . We choose a spatial domain wide enough to enclose all changes necessary for con-

sideration. In this case, we define our spatial domain with a length of $20 \mu\text{m}$, and the first exposure is set at $x = 5 \mu\text{m}$. As the photoresist is exposed to the laser beam, the photoinitiator gets excited and splits into two radicals, thus reducing its own concentration. We assume that the amount of excited photoinitiator molecules is proportional to the intensity of the exposure and the concentration of photoinitiator. Because the concentrations of species are hard, if not impossible, to determine experimentally, we assume arbitrary units for concentrations. Let α be the diffusivity of photoinitiator in the photoresist, $I(x)$ be the intensity function, $R(x)$ be the function that describes the intensity of reflections within the photoresist, and m be the conversion coefficient of photoinitiation with respect to beam intensity. Then the PDE that describes the concentration of photoinitiator is

$$c_t = \alpha \cdot c_{xx} - m \cdot (I(x) + R(x)) \cdot c, \quad (7.1)$$

with initial condition

$$c(x, 0) = 1, \quad (7.2)$$

and boundary conditions

$$c_x(0, t) = c_x(20, t) = 0. \quad (7.3)$$

It turns out, in the end, that the reflection term $R(x)$ plays an important role in this model of memory effect. Without this term, we were not able to obtain data for the percent increase that was comparable to the experimental results. A plot of the reflection term, $R(x)$, together with the beam intensity, $I(x)$, is given in Figure 7.1, where the blue curve shows the beam intensity and the purple curve shows the intensity due to reflection.

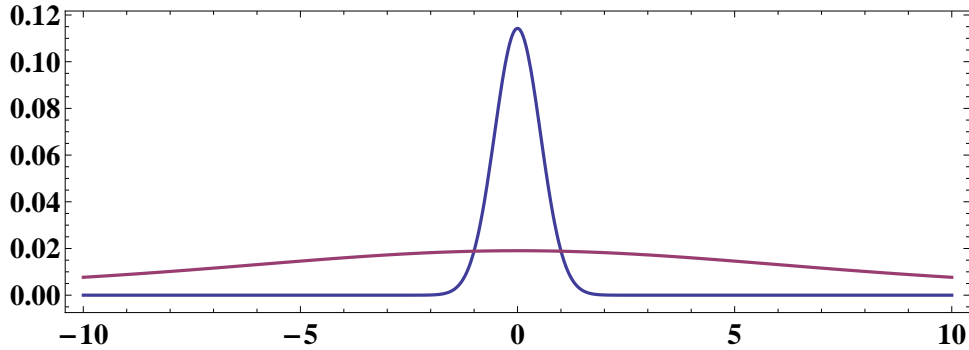


Figure 7.1: Beam Intensity $I(x)$ and Reflection Intensity $R(x)$

We convert this PDE into a difference equation with the method introduced in Section 5.3. Equation (7.1) can be rewritten into

$$\begin{aligned} \frac{c(k, n+1) - c(k, n)}{\Delta t} &= \alpha \cdot \frac{c(k+1, n) - 2c(k, n) + c(k-1, n)}{\Delta x^2} \\ &\quad - m \cdot (I(k\Delta x) + R(k\Delta x)) \cdot c(k, n). \end{aligned} \tag{7.4}$$

Solving for the future time step,

$$\begin{aligned} c(k, n+1) &= c(k, n) + \alpha \cdot \frac{\Delta t}{\Delta x^2} \cdot (c(k+1, n) - 2c(k, n) + c(k-1, n)) \\ &\quad - \Delta t \cdot m \cdot (I(k\Delta x) + R(k\Delta x)) \cdot c(k, n). \end{aligned} \tag{7.5}$$

The initial condition (7.2) can be converted into

$$c(k, 0) = 1. \tag{7.6}$$

Notice that we use Neumann boundary conditions for this approximation because we want to assume zero net flow of concentrations at the boundaries. This is different from the example given in Section 5.3, where we considered Dirichlet boundary conditions. There are several ways to treat the Neumann boundary conditions [Tho95]. For simplicity, we

would use a one-sided difference approximation of $c_x(0, t)$ to get

$$\frac{c(1, n+1) - c(0, n+1)}{\Delta x} = \frac{c(M, n+1) - c(M-1, n+1)}{\Delta x} = 0,$$

or, equivalently,

$$c(0, n+1) = c(1, n+1) \quad \text{and} \quad c(M, n+1) = c(M-1, n+1). \quad (7.7)$$

Thus, equations (7.5)–(7.7) approximate the differential equation described by equations (7.1)–(7.3).

7.2 Second Approximation: Acrylate Initiation

With a method similar to the last section, we can also approximate the concentration of radicals. This concentration is denoted $u(x, t)$ as a function of space x and time t on the same spatial domain $x \in [0, 20]$. The mechanism mentioned in Section 1.3 suggests that one molecule of photoinitiator gets excited and splits into two radicals. *Conservation of Mass* implies that the increase in radicals equals twice the consumption in photoinitiators. At the same time, radicals are not stable and tend to quench each other when they are placed in the same vessel. Hence, a sink term describing the decay of radicals is also included. Radical quenching always involve two radicals, which suggests that the quenching reaction is second-order. Thus the rate of decay, given by d , is proportional to the second power of radical concentration. Let β be the diffusivity of radicals. Then the

PDE describing the radical concentration is

$$u_t = \beta \cdot u_{xx} + 2m \cdot \left(I(x) + R(x) \right) \cdot c - d \cdot u^2, \quad (7.8)$$

with initial condition, while no radical should be present initially,

$$u(x, 0) = 0, \quad (7.9)$$

and boundary conditions

$$u_x(0, t) = u_x(20, t) = 0. \quad (7.10)$$

Notice that this PDE involves the concentration of photoinitiator $c(x, t)$. Thus it forms a coupled system of PDEs with equations (7.1)–(7.3). Its corresponding difference equation is

$$\begin{aligned} \frac{u(k, n+1) - u(k, n)}{\Delta t} &= \beta \cdot \frac{u(k+1, n) - 2u(k, n) + u(k-1, n)}{\Delta x^2} \\ &\quad + 2m \cdot \left(I(k\Delta x) + R(k\Delta x) \right) \cdot c(k, n) - d \cdot u^2(k, n), \end{aligned} \quad (7.11)$$

or, equivalently,

$$\begin{aligned} u(k, n+1) &= u(k, n) + \beta \cdot \frac{\Delta t}{\Delta x^2} \cdot \left(u(k+1, n) - 2u(k, n) + u(k-1, n) \right) \\ &\quad + \Delta t \cdot 2m \cdot \left(I(k\Delta x) + R(k\Delta x) \right) \cdot c(k, n) - \Delta t \cdot d \cdot u^2(k, n), \end{aligned} \quad (7.12)$$

with initial condition

$$u(k, 0) = 0, \quad (7.13)$$

and boundary conditions

$$u(0, n+1) = u(1, n+1) \quad \text{and} \quad u(M, n+1) = u(M-1, n+1). \quad (7.14)$$

Therefore, equations (7.5)–(7.7) and (7.12)–(7.14) form a coupled system of difference equations that describes the concentration of photoinitiator and radicals in the photoresist. Our next step is to model the process of polymerization using Markov chains.

7.3 Probability of Polymerization

We use the concept of Markov chains introduced in Section 5.4 to model the polymerization of the photoresist, in which case we consider the particle to be the boundaries of the polymer. It simplifies the two-dimensional polymerization by modeling along the one-dimensional line connecting two exposure centers. A jump to the right to be polymerization over one spatial unit, and no jump as no growth in the polymer. Then the states of this Markov chain are the possible positions for the left and right boundaries of the polymer, and the transition probability is the probability of polymerization given the radical concentration at the position of the boundary. We first define the transition probability $p(u)$, *i.e.*, probability of polymerization, as a function of radical concentration u .

First of all, we expect there to be a threshold on the radical concentration that governs the polymerization reaction: higher than the threshold concentration, polymerization is likely to occur, and *vice versa*. Then we consider the extremes: when the radical concentration is close to zero, the probability of polymerization is expected to be close to 0; when the radical concentration is very high, the probability of polymerization is

expected to be close to 1. Finally, we expect a smooth transition near the threshold concentration. In conclusion, a probability of polymerization $p(u)$ as a function of radical concentration u is expected to have a plot resembling Figure 7.2a. Note that the plot of the probability function resembles the phase paths of the differential equation $y' = ky(1 - y)$, where k is a positive constant.

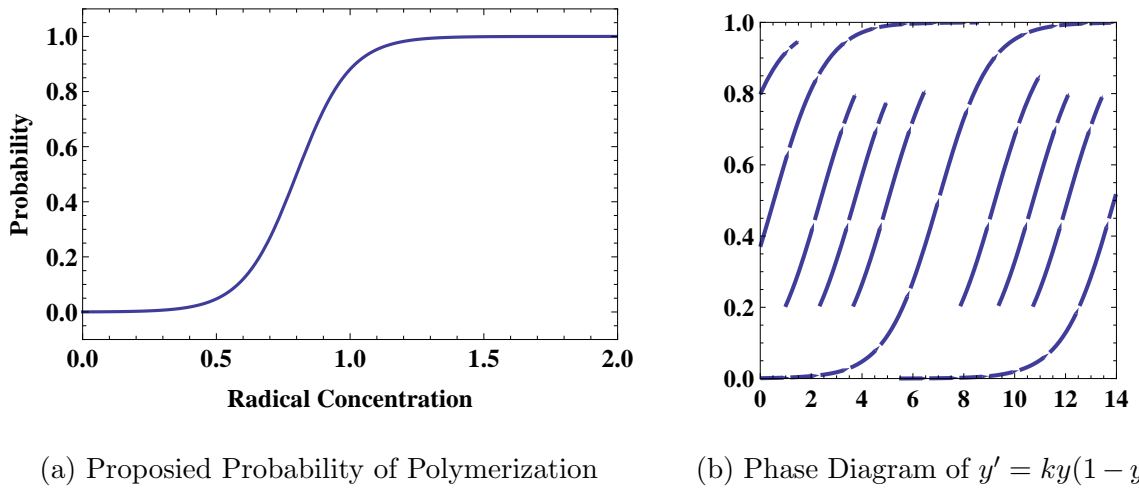


Figure 7.2: Modeling the Probability Function

The general solutions to the differential equation $y' = ky(1 - y)$ is

$$y(x) = \frac{1}{1 + e^{c-kx}}, \quad (7.15)$$

where c and k are constants, and $k > 0$. A derivation of the solutions to this differential equation is provided in Appendix F.

Now we obtain our probability of polymerization $p(u)$ as a function of radical concentration u :

$$p(u) = \frac{1}{1 + e^{c-ku}}, \quad (7.16)$$

where the constant k controls the “steepness” of the transition between 0 and 1, and the ratio of c and k controls the threshold concentration for polymerization. We shall proceed to use this probability of polymerization for Markov modeling.

7.4 Third Approximation: Markov Modeling

The Markov model is based on the difference model described in Sections 7.1 and 7.2. We define $P_l(k, n)$ and $P_r(k, n)$ as the probability of the left and right boundaries, respectively, to be at the k -th spatial unit at the n -th time step, where k is an integer between 0 and M , and n is a non-negative integer. The polymerization is expected to start at the center of exposure $x = 5 \mu\text{m}$. It follows that the initial conditions for the probability density functions of the left and right boundaries, $P_l(k, n)$ and $P_r(k, n)$, respectively, should be defined by

$$P_l(k, 0) = P_r(k, 0) = \begin{cases} 1, & \text{if } k\Delta x \leq 5 < (k+1)\Delta x, \\ 0, & \text{otherwise.} \end{cases} \quad (7.17)$$

Because most of the cases that we experimentally tested did not yield dot size greater than $10 \mu\text{m}$, it is safe to assume the boundary conditions

$$P_l(0, n) = P_l(M, n) = 0, \quad \text{and} \quad P_r(0, n) = P_r(M, n) = 0. \quad (7.18)$$

The discrete probability density functions are updated during each time iteration according to equation (5.23). Since we have derived the probability of polymerization with

respect to radical concentration, we may rewrite the equation into

$$P_l(k, n+1) = P_l(k, n) \cdot \left(1 - p(u(k, n))\right) + P_l(k+1, n) \cdot p(u(k+1, n)), \quad (7.19)$$

and

$$P_r(k, n+1) = P_r(k, n) \cdot \left(1 - p(u(k, n))\right) + P_r(k-1, n) \cdot p(u(k-1, n)). \quad (7.20)$$

With equations (7.17)–(7.20), we are able to obtain the discrete probability density functions $P_l(k, n)$ and $P_r(k, n)$, which describe the positions of the left and right boundaries of the polymer at any time step. With the probability density functions, the *expected values* of the boundary positions can be computed by equation (5.24). We model the second exposure in the same way, except that we need to use different initial conditions in (7.21)–(7.23) according to the spacing between two exposures.

$$c_{\text{second}}(k, 0) = c_{\text{first}}(k, \text{FinalTimeIteration}) \quad (7.21)$$

$$u_{\text{second}}(k, 0) = u_{\text{first}}(k, \text{FinalTimeIteration}) \quad (7.22)$$

$$P_l(k, 0) = P_r(k, 0) = \begin{cases} 1, & \text{if } k\Delta x \leq 5 + \text{Spacing} < (k+1)\Delta x, \\ 0, & \text{otherwise.} \end{cases} \quad (7.23)$$

Significant changes in physical properties take place when the acrylate-based photoresist turns into polymer. The index of refraction changes when the photoresist turns from a liquid to a solid, and thus we are able to see the polymer under the microscope. Moreover, the diffusivity changes dramatically because it is hard for particles to flow within solid state matters. The diffusive behaviors are therefore turned off by setting the diffusivity coefficients α and β to zero between the boundaries of the polymer.

Chapter 8

Mathematica Implementation

In this chapter, we first develop a framework of the implementation in Mathematica by programming the model for the system of PDEs that describes the concentrations of photoinitiator and radicals. Then we use the framework to implement the markov model into the program. The result of the model is compared with the experimentally-determined data to evaluate the validity of the model.

8.1 Finite Difference Modeling

The program starts by setting up all the parameters and variables for the beam profile and exposure. The initial conditions of c and u are set with a `For` loop which generates two lists `initc` and `initu` of length $M + 1$ consisting of 1's and 0's, respectively. These two lists are appended into c and u , respectively, as the initial time iteration.

A new `For` loop is used for time iterations. At the start of each time iteration, empty lists `cnew` and `unew` are generated for storing the values of concentration during the current time iteration. Another `For` loop is then used for spatial iterations, which puts the concentration values into the lists `cnew` and `unew`. An `If` statement checks whether the current spatial grid is at the boundary and, if it is, the `If` statement makes changes to preserve the boundary conditions. At the end of each time iteration, the completed lists `cnew` and `unew` are appended to lists `c` and `u`, respectively.

When all the time iterations are completed, a `Manipulate` command, together with a `ListLinePlot`, is used to show the change in the concentration of species during the time period which the program simulated.

8.2 Markov Modeling

The implementation of Markov modeling inherits the framework set up in the previous section. In addition to the initial conditions for `c` and `u`, we also need to include the initial conditions for `pLeft` and `pRight`. Moreover, we introduce another list `Poly` to keep track of the polymerized spatial units so that we are able to turn off diffusive behaviors in these units. The content of this list is essentially only 0's and 1's, where a 0 means not polymerized and 1 polymerized for the corresponding spatial grid.

In the `For` loop for time iteration, two new lists `pnewLeft` and `pnewRight` are constructed in the same fashion as we construct `c` and `u`, and appended to `pLeft` and `pRight`,

respectively, at the end of each time iteration. The expected values of left and right boundaries are calculated after `pnewLeft` and `pnewRight` are generated, and an update of `newPoly`, which has 1's between the expected boundaries and 0's elsewhere, is appended to `Poly`. For the second exposure, the initial conditions for `c`, `u`, and `Poly` are the same as their final states during the simulation for the first exposure, but the initial conditions for `pLeft` and `pRight` have to be reset to the new exposure center because we cannot have four boundaries for a growing polymer.

The `Manipulate` command is modified so that the expected boundaries of the polymer dots are visible in the simulation. In addition, the number of polymerized spatial units are printed as the output at the end of the simulation for each exposure. The percent increase is also calculated at the very end of the program.

Pseudocodes for the complete implementation is provided in the next section. Additionally, a completed version of the program in Wolfram Mathematica® 8 is provided in Appendix D. The code is fragmented into functional modules and arranged as sections of the appendix. The indices of lists in the code are off by 1 because we started our indices at 0 but Mathematica takes 1 as the index of the first item of a list structure.

8.3 Pseudocode for the Implementation

The pseudocode for modeling the polymerization under a double exposure is included in the next page to demonstrate the flow of the program.

Parameters

```

 $c \leftarrow \{initc\}, u \leftarrow \{initu\},$                                 ▷ Set up the adjustable parameters
 $pLeft \leftarrow \{initp\}, pRight \leftarrow \{initp\}, Poly \leftarrow \{initPoly\},$ 
 $\text{for } n \leftarrow 1, n\Delta t \leq FinalTime \text{ do}$                       ▷ Set up the initial conditions
 $cnew = unew = pnewLeft = pnewRight = \{\}$                                ▷ Time iteration
 $\text{for } k \leftarrow 0, k \leq M \text{ do}$                                      ▷ Spatial iteration
 $\text{if } Poly(k) = 1 \text{ then}$ 
    Set  $\alpha$  and  $\beta$  to be zero in this spatial iteration
 $\text{end if}$ 
 $\text{if } k = 0 \text{ or } k = M \text{ then}$ 
    Update  $cnew, unew, pnewLeft, pnewRight$  according to boundary conditions
    i.e. equations (7.7), (7.14), and (7.18)
 $\text{else}$ 
    Update  $cnew, unew, pnewLeft, pnewRight$  according to difference equations
    i.e. equations (7.5), (7.12), (7.19), and (7.20)
 $\text{end if}$ 
 $\text{end for}$ 
Append  $cnew, unew, pnewLeft, pnewRight$  to  $c, u, pLeft, pRight$ , respectively
Compute the expectation values  $leftExpect$  and  $rightExpect$  of the boundaries
 $Polynew \leftarrow \{1 \text{ within } leftExpect \text{ and } rightExpect, 0 \text{ otherwise}\}$ 
Append  $Polynew$  to  $Poly$ 
 $\text{end for}$ 
 $\text{return } Dot1 \leftarrow \# \text{ of } 1\text{'s in the final state of } Poly$                 ▷ Dot 1 size

```

Set up the initial condition for the second exposure

```

 $\text{for } n \leftarrow 1, n\Delta t \leq FinalTime \text{ do}$                       ▷ Final state of the first exposure
    Exactly the same for loop with the first one
 $\text{end for}$ 
 $\text{return } Dot2 \leftarrow \# \text{ of } 1\text{'s in the final state of } Poly - Dot1$         ▷ Dot 2 size
 $\text{return } percentIncrease \leftarrow (Dot2 - Dot1)/Dot1$ 

```

Manipulate command that shows the dynamics of polymerization

8.4 Results and Discussion

The parameters of the model were adjusted to fit the experimental data provided in Table 6.2. Table 8.1 shows the chosen values of all the adjustable parameters and functions used in the final version of the model. The first dot of each experiment has 0.5-second exposure, and we assume the second exposure does not affect the size of the first dot.

Parameters or Functions	Values of Choice
z	$1 \mu\text{m}$
α	$0.2 \mu\text{m}^2/\text{s}$
β	$0.1 \mu\text{m}^2/\text{s}$
m	$400 \text{ s}^{-1}/I_0$
d	$0.3 \text{ AU}^{-1} \cdot \text{s}^{-1}$
$R(x)$	$\frac{I(x/20) + I(x/10)}{12}$
$p(u)$	$\frac{1}{1 + e^{20-25u}}$

Table 8.1: Choices for Parameters and Functions

Then we compute the average size of the first dot to be $2.1 \pm 0.3 \mu\text{m}$. This size was measured under SEM, thus after shrinkage. If we account for the shrinkage coefficient of photoresist #3 (25%, Table 3.2), the average dot size before shrinkage would be $2.8 \pm 0.4 \mu\text{m}$. After painstaking efforts on adjusting the parameters, we achieved $2.76 \mu\text{m}$ for the size of the first dot computed by the model. The dot sizes simulated by the model are provided in Table 8.2. The simulation of experiment #2 is provided in Figure 8.1 by one

#	Spacing (μm)	1 st exposure (s)	2 nd exposure (s)	Hiatus time (s)	1 st Dot (# grids)	2 nd Dot (# grids)	% Increase
1	10	0.50	0.50	2.0	69	76	10%
2	10	0.50	0.50	1.0	69	87	26%
3	10	0.50	0.50	0.54	69	98	42%
4	8	0.50	0.50	2.0	69	77	12%
5	8	0.50	0.50	1.0	69	94	36%
6	8	0.50	0.56	0.50	69	118	71%
7	5	0.50	0.54	2.0	69	79	14%
8	5	0.50	0.56	1.0	69	123	78%
9	5	0.50	0.50	0.50	69	—	—

Table 8.2: Percent Increase Results Simulated by the Model

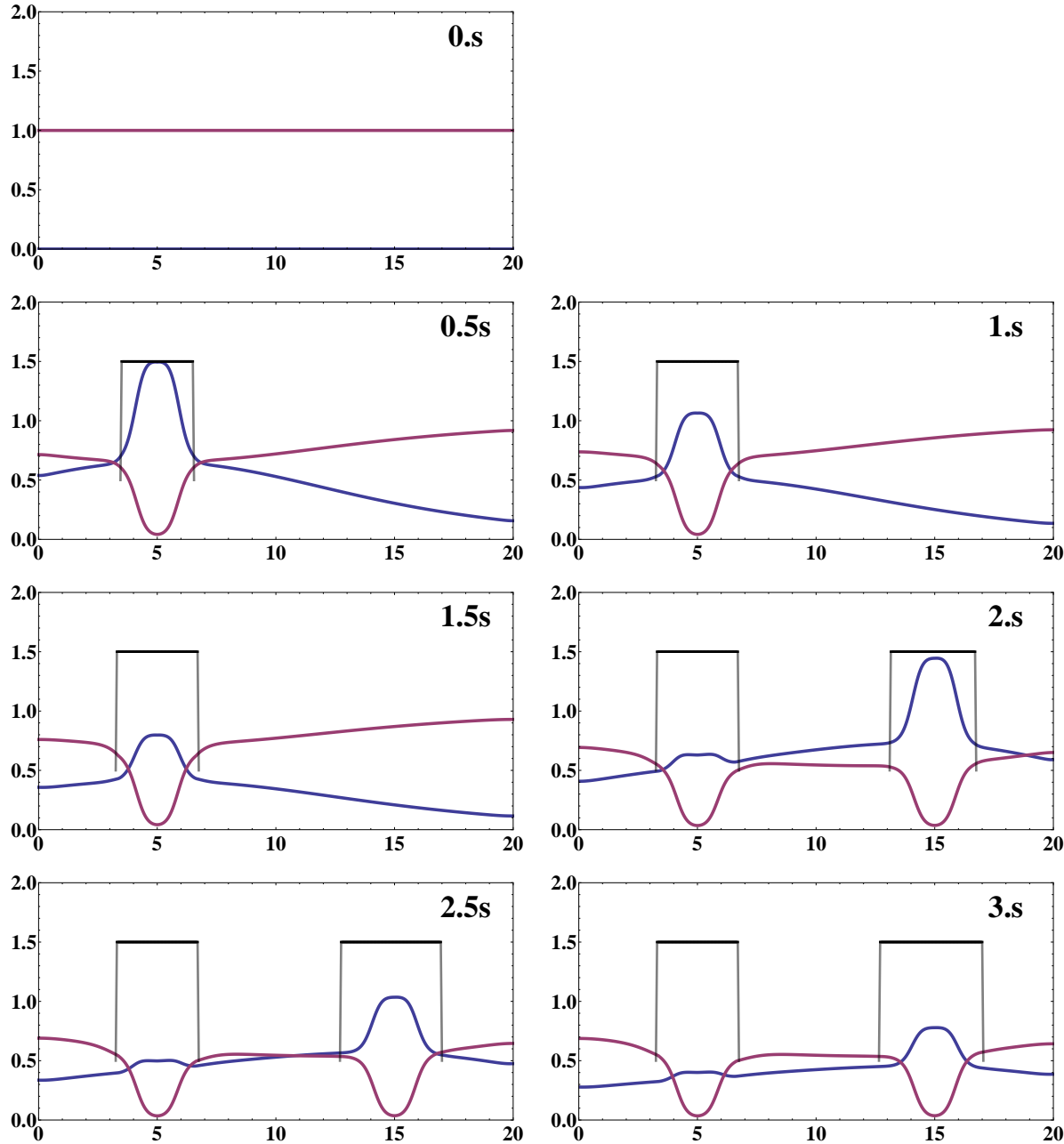


Figure 8.1: Simulation Result of Experiment #2

screenshot every 0.5 second. The blue and purple lines in the diagrams indicate the concentrations (arbitrary unit) of radicals and photoinitiator, respectively. The black boxes indicate the size of the growing polymer. A more detailed simulation of this experiment is provided in Appendix E with one screenshot every 0.1 second.

The percent increase values simulated by the model and the experimentally-determined values are tabulated in Table 8.3. Both sets of data showed the same pattern. The memory effect is stronger at places close to the exposed areas, and is reduced far away from fabricated structures. The memory effect is also stronger immediately after one exposure, and if we wait a while after an exposure, memory effect can be reduced.

#	1	2	3	4	5	6	7	8	9
Experimental	15%	24%	32%	19%	29%	47%	21%	—	—
Modeling	10%	26%	42%	12%	36%	71%	14%	78%	—

Table 8.3: Comparison between Experiments and the Model

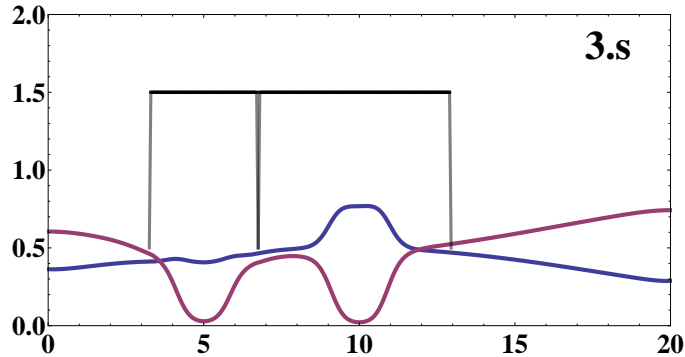


Figure 8.2: Final State of Simulation #8

We notice that the experimental data #8 showed two dots merged together due to their proximity (Figure C.8), yet the model still suggested two distinct dots. But if we take a closer look at the final state of the model (Figure 8.2), the distance between two boundaries is only 1 spatial unit, which converts to 50 nm. This distance is so small that we can consider the dots as merged together.

8.5 Future Development

First of all, we can tune the parameters and adjustable function in the model more carefully and more finely to make the outputs of the model closer to the experimental values. We may also test the model for double-dot experiments with different laser power and/or different exposure time.

We have successfully used a radical scavenger ingredient for the photoresist to reduce the linewidth as well as the memory effect. We have also developed a model describing the polymerization reaction with double dots. The natural step to follow would be modeling memory effect in the photoresist without the radical scavenger. By comparing the differences in these two models, we may be able to suggest the role of radical scavenger in reducing linewidth and memory effect.

Another possible direction to go would be taking the model into higher dimensions. Currently the model describes the polymerization reaction along the line connecting two exposures, which has only one spatial dimension. It is possible that we can develop a two-

dimensional model which tells the polymerization on a plane. Given specific fabrication conditions, the two-dimensional model may be able to simulate the outcome of a DLW experiment before actually running the experiment.

Appendix A

Linewidths before/after Alcohol Development

Linewidth Measurements of Photoresist #1

Before (μm)	46.8	50.2	53.6	58.1	62.7	65.9	69.9	73.8
After (μm)	34.63	37.94	41.33	45.02	49.57	52.77	56.06	59.38
Before (μm)	77.3	78.6	82.2	85.8	89.9	93.0	97.7	101.0
After (μm)	62.28	63.04	66.38	69.64	72.90	76.12	80.59	83.51
Before (μm)	104.9	108.3	114.0	117.7	121.8	124.8	137.7	141.8
After (μm)	86.86	89.50	94.22	97.21	99.15	102.71	123.17	127.42
Before (μm)	145.1	149.4	153.6	154.4	159.7	163.5	166.9	170.5
After (μm)	130.94	134.60	138.23	138.61	142.87	146.39	150.97	153.02
Before (μm)	175.4	179.5	183.9	187.1				
After (μm)	156.56	160.88	163.65	167.08				

Table A.1: Linewidths before and after developing (photoresist #1)

Linewidth Measurements of Photoresist #2

Before (μm)	60.7	64.5	69.7	72.8	77.1	78.5	81.7	85.5
After (μm)	48.46	52.55	56.54	59.81	63.56	64.77	68.70	72.40
Before (μm)	89.4	94.1	94.4	98.9	102.2	106.6	111.6	111.0
After (μm)	75.90	80.14	80.58	84.81	88.84	92.01	96.02	95.88
Before (μm)	114.9	119.2	122.4	125.9	127.0	131.4	135.5	139.2
After (μm)	99.66	103.56	107.14	109.94	111.36	114.94	118.50	121.97
Before (μm)	142.4	143.9	148.7	151.6	155.1	157.5	158.7	161.9
After (μm)	124.91	126.32	130.53	133.66	137.14	139.84	141.27	144.29
Before (μm)	166.2	169.0	173.0	174.9	177.7	182.0	185.8	189.8
After (μm)	147.83	150.16	153.46	155.28	157.78	161.31	165.49	168.12

Table A.2: Linewidths before and after developing (photoresist #2)

Linewidth Measurements of Photoresist #3

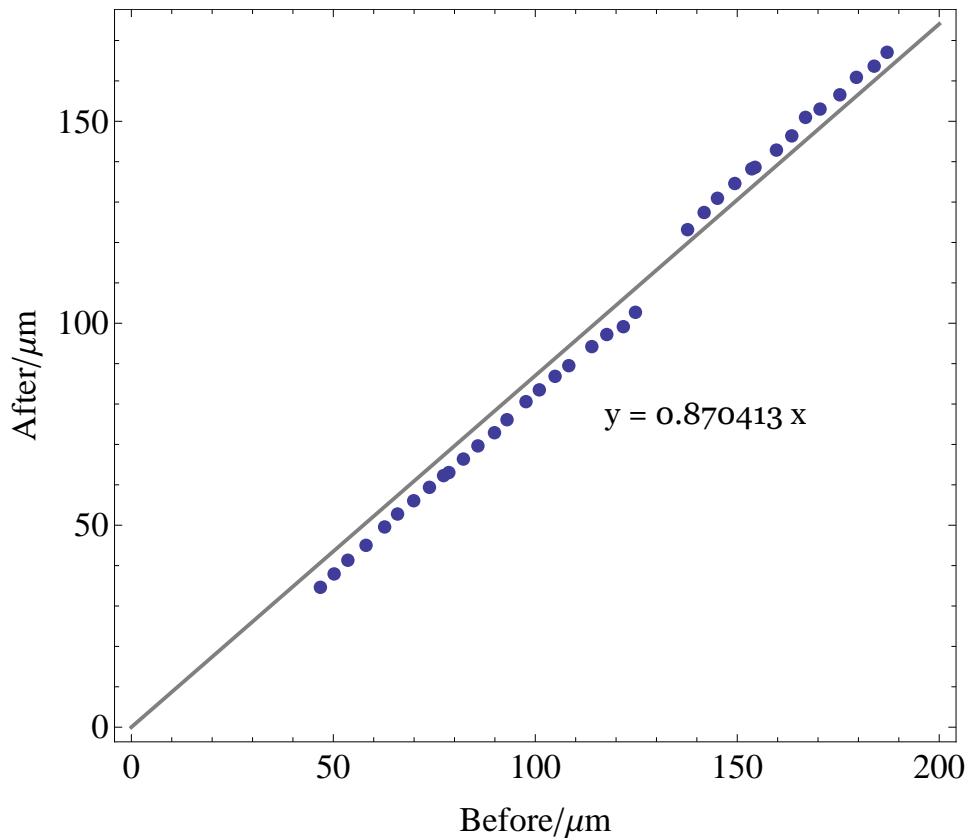
Before (μm)	57.5	61.2	64.5	68.4	71.8	73.4	78.1	81.0
After (μm)	46.63	50.89	54.02	56.90	59.56	62.33	66.18	69.23
Before (μm)	84.8	87.4	89.7	93.7	97.8	100.8	104.2	106.1
After (μm)	72.42	75.01	77.13	81.13	84.15	87.66	89.95	91.71
Before (μm)	110.1	113.8	117.5	120.8	122.8	125.3	129.4	133.3
After (μm)	95.66	98.88	102.43	103.98	106.72	108.67	113.05	116.40
Before (μm)	136.7	138.7	142.3	146.3	149.9	153.2	154.5	157.7
After (μm)	117.32	119.46	122.38	128.05	129.86	131.53	131.24	135.63
Before (μm)	162.0	165.2	168.1	169.4	173.4	177.1	180.5	183.9
After (μm)	138.68	141.18	143.01	143.45	146.68	149.52	153.05	155.39

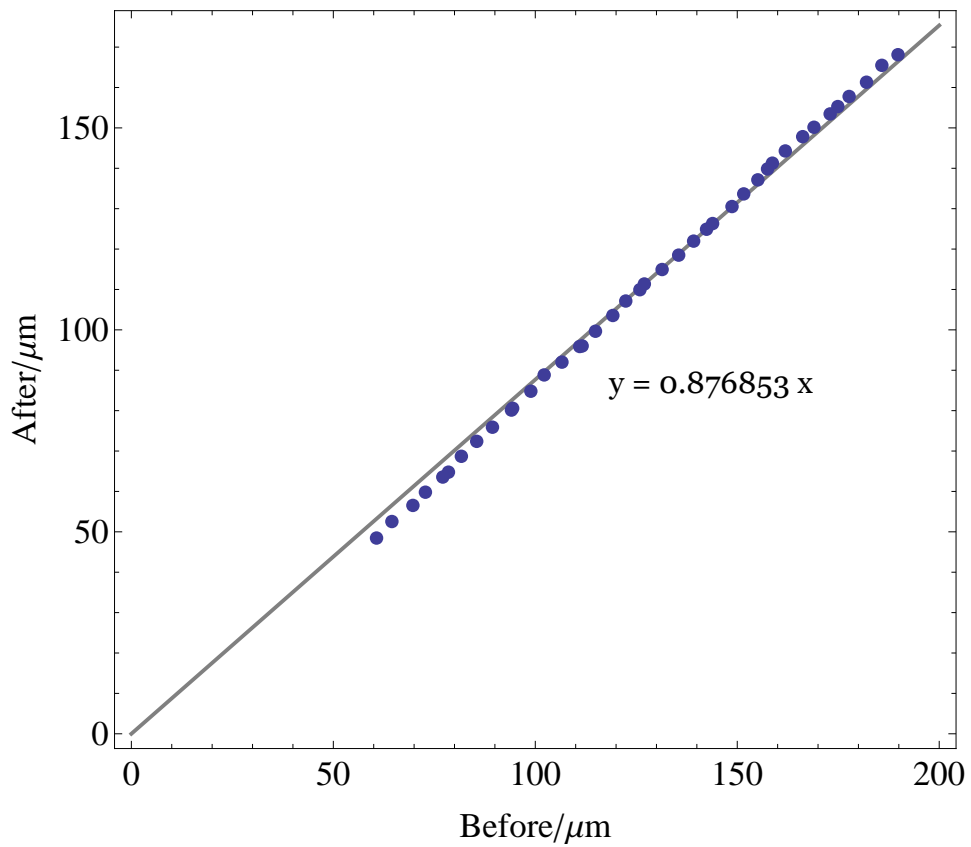
Table A.3: Linewidths before and after developing (photoresist #3)

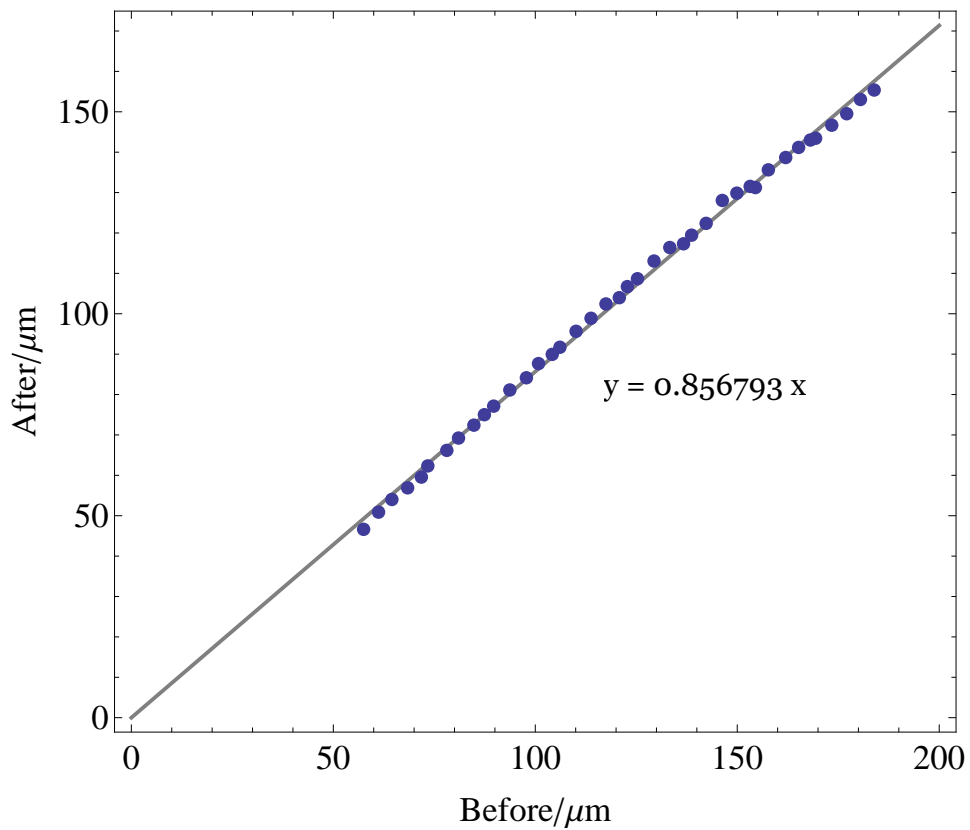
Linewidth Measurements of Photoresist #4

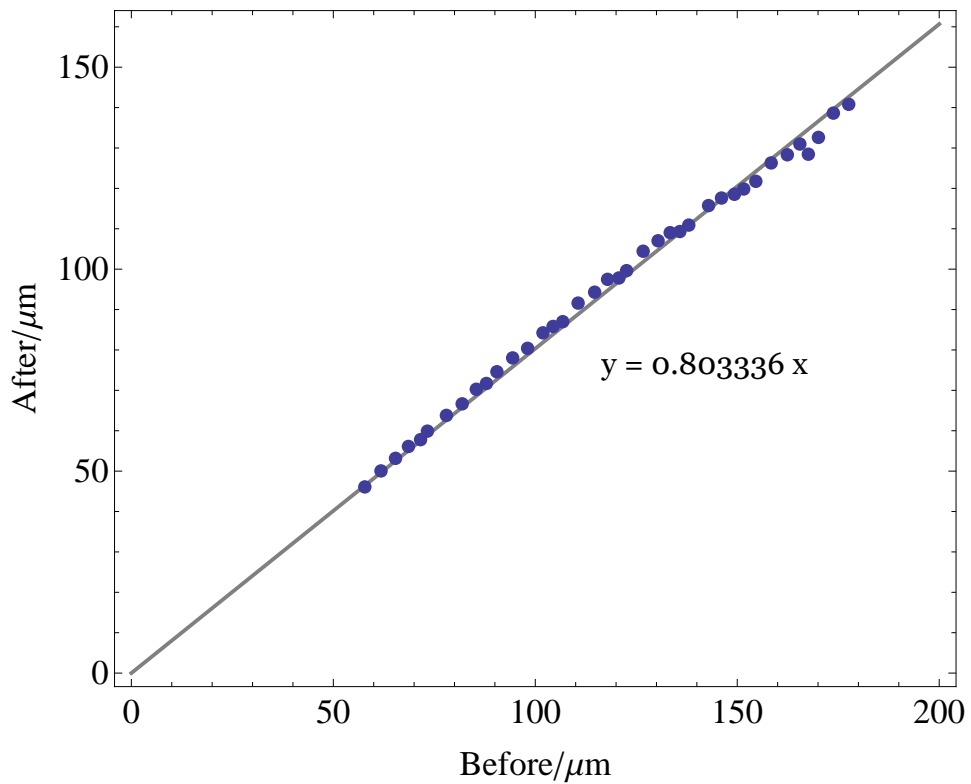
Before (μm)	57.8	61.8	65.4	68.6	71.6	73.3	78.0	81.9
After (μm)	46.09	50.05	53.17	56.11	57.79	59.90	63.80	66.66
Before (μm)	85.4	87.9	90.5	94.4	98.1	101.9	104.4	106.8
After (μm)	70.27	71.70	74.60	78.03	80.40	84.24	85.82	87.00
Before (μm)	110.6	114.7	117.9	120.7	122.6	126.7	130.4	133.4
After (μm)	91.60	94.30	97.48	97.82	99.63	104.44	107.03	109.03
Before (μm)	135.8	138.0	142.9	146.1	149.3	151.6	154.6	158.4
After (μm)	109.32	110.91	115.74	117.61	118.54	119.85	121.75	126.30
Before (μm)	162.4	165.5	167.6	170.1	173.8	177.6		
After (μm)	128.32	130.98	128.46	132.62	138.63	140.81		

Table A.4: Linewidths before and after developing (photoresist #4)

Figure A.1: Linewidth after *v.s.* before developing (photoresist #1)

Figure A.2: Linewidth after *v.s.* before developing (photoresist #2)

Figure A.3: Linewidth after *v.s.* before developing (photoresist #3)

Figure A.4: Linewidth after *v.s.* before developing (photoresist #4)

Appendix B

Linewidth Data with Different DLW

Conditions

Linewidth Measurement Data for Photoresist #1

Linewidth (μm)	Speed ($\mu\text{m}/\text{s}$)				Linewidth (μm)	Speed ($\mu\text{m}/\text{s}$)							
	20	30	40	50		20	30	40	50				
100 nW	#1	1.39	0.78	0.64	0.57	#1	2.27	1.88	1.46	1.16			
	#2	1.66	0.88	0.65	0.55	#2	2.66	1.89	1.31	1.10			
	#3	2.07	0.83	0.72	0.54	#3	2.68	1.98	1.33	1.14			
	#4	1.94	0.87	0.73	0.56	#4	2.59	2.15	1.47	1.09			
	#5	1.92	0.92	0.68	0.59	#5	2.54	2.21	1.56	1.18			
Average		1.80	0.86	0.68	0.56	Average				2.55	2.02	1.43	1.13

(a) 100 nW

(b) 150 nW

Linewidth (μm)	Speed ($\mu\text{m}/\text{s}$)				Linewidth (μm)	Speed ($\mu\text{m}/\text{s}$)							
	20	30	40	50		20	30	40	50				
200 nW	#1	3.66	3.03	2.72	1.69	#1	4.35	3.19	2.44	1.58			
	#2	3.81	3.10	2.93	1.54	#2	4.46	3.10	2.63	1.67			
	#3	3.83	3.31	2.97	1.60	#3	4.36	3.32	2.47	1.62			
	#4	3.58	3.37	2.78	1.64	#4	4.39	3.25	2.46	1.68			
	#5	3.77	3.41	2.97	1.56	#5	4.84	3.29	2.76	1.75			
Average		3.73	3.24	2.87	1.61	Average				4.48	3.23	2.55	1.66

(c) 200 nW

(d) 250 nW

Table B.1: Linewidth Measurement Data for Photoresist #1

Linewidth Measurement Data for Photoresist #2

Linewidth (μm)	Speed (μm/s)				Linewidth (μm)	Speed (μm/s)					
	20	30	40	50		20	30	40	50		
100 nW	#1	1.34	0.90	0.58	N/A	#1	1.28	1.09	0.62	0.54	
	#2	1.40	1.04	0.66	N/A	#2	1.38	1.37	0.79	0.59	
	#3	1.34	0.97	0.61	N/A	#3	1.43	1.08	0.72	0.56	
	#4	1.23	0.88	0.50	N/A	#4	1.44	0.89	0.63	0.51	
	#5	1.22	0.87	0.53	N/A	#5	1.44	1.01	0.66	0.54	
Average		1.31	0.93	0.58	N/A	Average		1.39	1.09	0.68	0.55

(a) 100 nW

(b) 150 nW

Linewidth (μm)	Speed (μm/s)				Linewidth (μm)	Speed (μm/s)					
	20	30	40	50		20	30	40	50		
200 nW	#1	1.89	1.29	0.98	0.81	#1	2.00	1.30	1.04	0.61	
	#2	2.06	1.44	1.00	0.77	#2	1.98	1.52	0.96	0.70	
	#3	2.10	1.35	0.97	0.80	#3	2.26	1.35	0.98	0.66	
	#4	1.97	1.32	0.98	0.80	#4	2.17	1.38	0.94	0.66	
	#5	1.98	1.31	0.94	0.81	#5	2.17	1.37	0.95	0.68	
Average		2.00	1.34	0.97	0.80	Average		2.12	1.38	0.97	0.66

(c) 200 nW

(d) 250 nW

Table B.2: Linewidth Measurement Data for Photoresist #2

Linewidth Measurement Data for Photoresist #3

Linewidth (μm)	Speed ($\mu\text{m}/\text{s}$)				Linewidth (μm)	Speed ($\mu\text{m}/\text{s}$)				
	20	30	40	50		20	30	40	50	
100 nW	#1	0.91	N/A	N/A	N/A	#1	1.05	0.92	0.83	0.80
	#2	1.05	N/A	N/A	N/A	#2	1.21	0.95	0.92	0.78
	#3	1.06	N/A	N/A	N/A	#3	1.24	0.98	0.93	0.83
	#4	0.83	N/A	N/A	N/A	#4	1.14	0.95	0.80	0.72
	#5	0.92	N/A	N/A	N/A	#5	1.10	0.98	0.83	0.70
Average		0.95	N/A	N/A	N/A	Average	1.15	0.96	0.86	0.77

(a) 100 nW

(b) 150 nW

Linewidth (μm)	Speed ($\mu\text{m}/\text{s}$)				Linewidth (μm)	Speed ($\mu\text{m}/\text{s}$)				
	20	30	40	50		20	30	40	50	
200 nW	#1	1.50	0.88	0.55	0.41	#1	2.04	1.40	1.20	1.13
	#2	1.51	0.97	0.66	0.44	#2	2.03	1.48	1.19	1.06
	#3	1.63	1.00	0.60	0.39	#3	2.08	1.37	1.27	0.99
	#4	1.79	0.91	0.60	0.41	#4	2.04	1.51	1.38	1.07
	#5	1.67	0.93	0.58	0.44	#5	2.12	1.46	1.31	1.02
Average		1.62	0.94	0.60	0.42	Average	2.06	1.44	1.27	1.05

(c) 200 nW

(d) 250 nW

Table B.3: Linewidth Measurement Data for Photoresist #3

Linewidth Measurement Data for Photoresist #4

Linewidth (μm)	Speed ($\mu\text{m}/\text{s}$)				Linewidth (μm)	Speed ($\mu\text{m}/\text{s}$)				
	20	30	40	50		20	30	40	50	
100 nW	#1	N/A	N/A	N/A	N/A	#1	0.96	0.89	0.56	0.57
	#2	N/A	N/A	N/A	N/A	#2	1.04	0.81	0.62	0.58
	#3	N/A	N/A	N/A	N/A	#3	1.03	0.85	0.66	0.59
	#4	N/A	N/A	N/A	N/A	#4	1.12	0.94	0.68	0.67
	#5	N/A	N/A	N/A	N/A	#5	1.14	0.92	0.72	0.69
Average	N/A N/A N/A N/A				Average	1.06 0.88 0.65 0.62				

(a) 100 nW

(b) 150 nW

Linewidth (μm)	Speed ($\mu\text{m}/\text{s}$)				Linewidth (μm)	Speed ($\mu\text{m}/\text{s}$)				
	20	30	40	50		20	30	40	50	
200 nW	#1	0.97	0.72	0.70	0.59	#1	2.04	1.32	1.03	0.84
	#2	1.15	0.82	0.59	0.62	#2	2.06	1.42	1.12	0.80
	#3	1.18	0.84	0.74	0.66	#3	1.86	1.58	1.25	0.91
	#4	1.16	0.83	0.64	0.51	#4	1.93	1.61	1.20	0.86
	#5	1.16	0.95	0.71	0.69	#5	1.97	1.37	1.09	0.85
Average	1.12 0.83 0.68 0.61				Average	1.97 1.46 1.14 0.85				

(c) 200 nW

(d) 250 nW

Table B.4: Linewidth Measurement Data for Photoresist #4

Linewidth		Speed ($\mu\text{m}/\text{s}$)				Linewidth		Speed ($\mu\text{m}/\text{s}$)			
Power (nW)	(μm)	20	30	40	50	Power (nW)	(μm)	20	30	40	50
	100	1.80	0.86	0.68	0.56		100	1.31	0.93	0.58	n/a
	150	2.55	2.02	1.43	1.13		150	1.39	1.09	0.68	0.55
	200	3.73	3.24	2.87	1.61		200	2.00	1.34	0.97	0.80
	250	4.48	3.23	2.55	1.66		250	2.12	1.38	0.97	0.66

(a) Photoresist #1	(b) Photoresist #2
--------------------	--------------------

Linewidth		Speed ($\mu\text{m}/\text{s}$)				Linewidth		Speed ($\mu\text{m}/\text{s}$)			
Power (nW)	(μm)	20	30	40	50	Power (nW)	(μm)	20	30	40	50
	100	0.95	n/a	n/a	n/a		100	n/a	n/a	n/a	n/a
	150	1.15	0.96	0.86	0.77		150	1.06	0.88	0.65	0.62
	200	1.62	0.94	0.60	0.42		200	1.12	0.83	0.68	0.61
	250	2.06	1.44	1.27	1.05		250	1.97	1.46	1.14	0.85

(c) Photoresist #3	(d) Photoresist #4
--------------------	--------------------

Table B.5: Linewidth Obtained from Different Fabricating Conditions

Appendix C

SEM Images of Double Dots

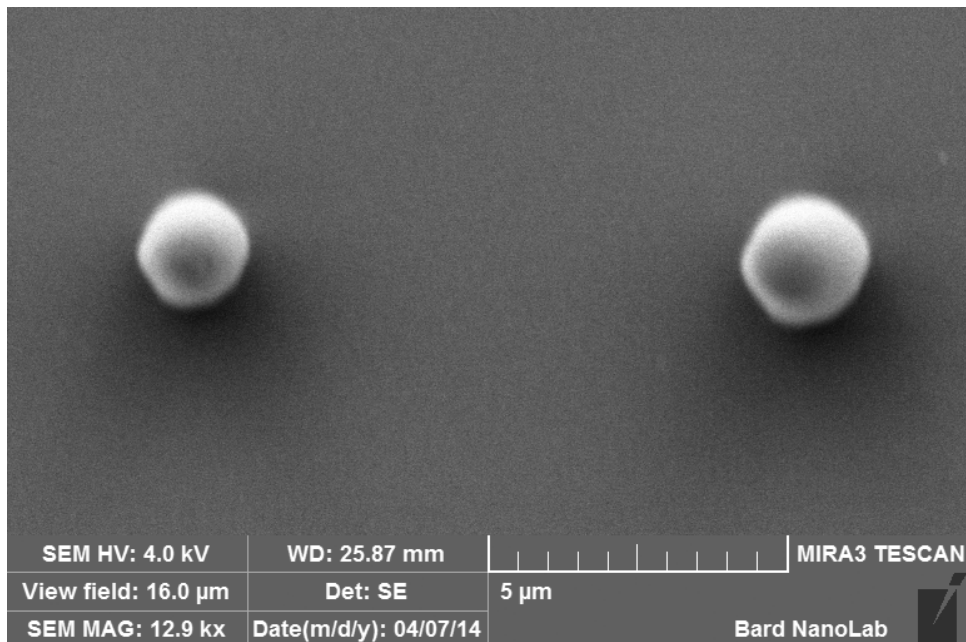


Figure C.1: SEM Image of Double-Dot Experiment #1

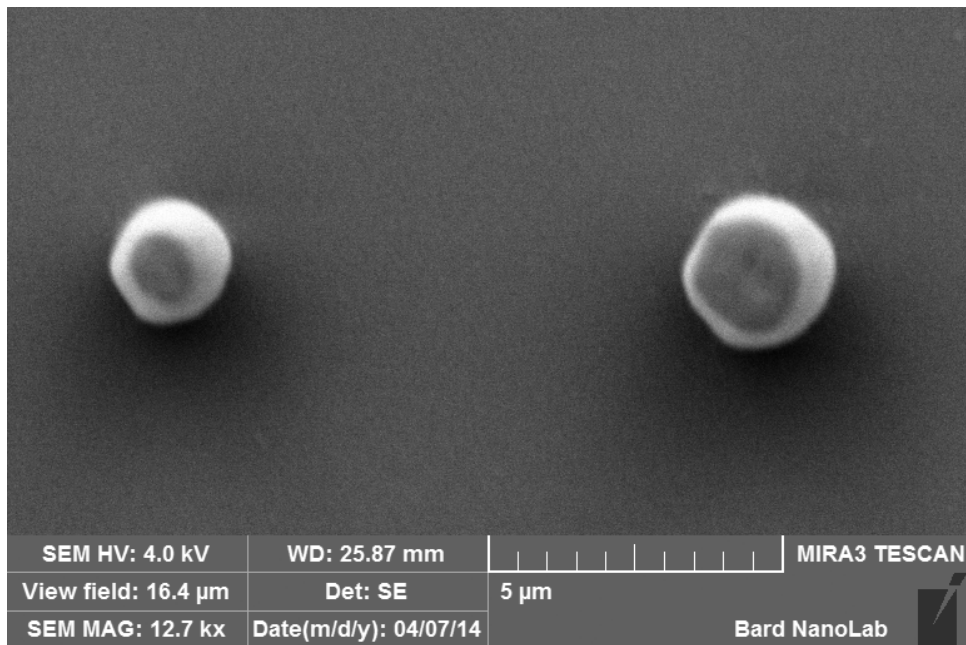


Figure C.2: SEM Image of Double-Dot Experiment #2

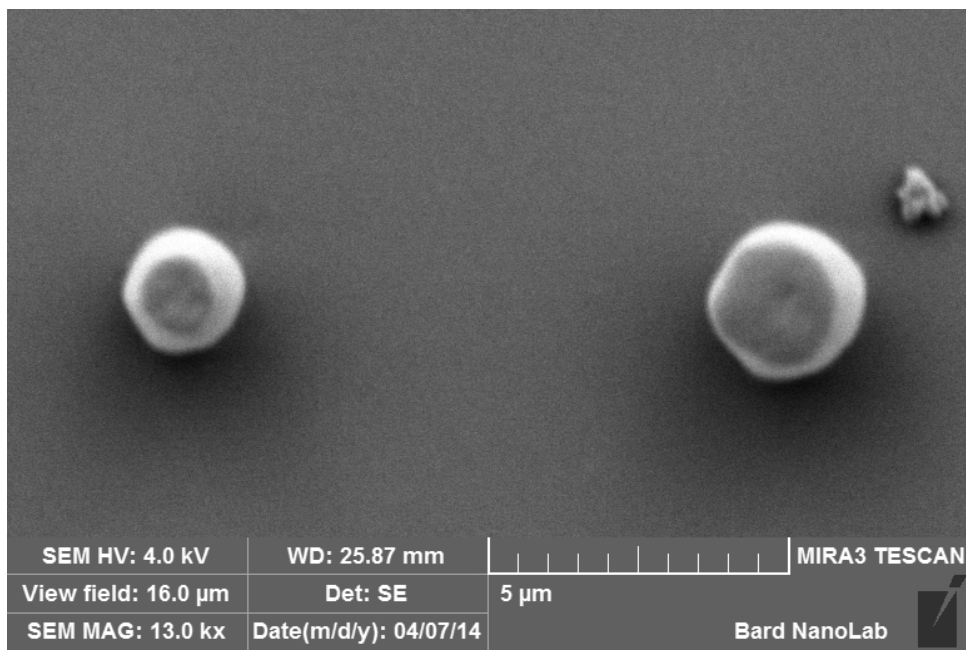


Figure C.3: SEM Image of Double-Dot Experiment #3

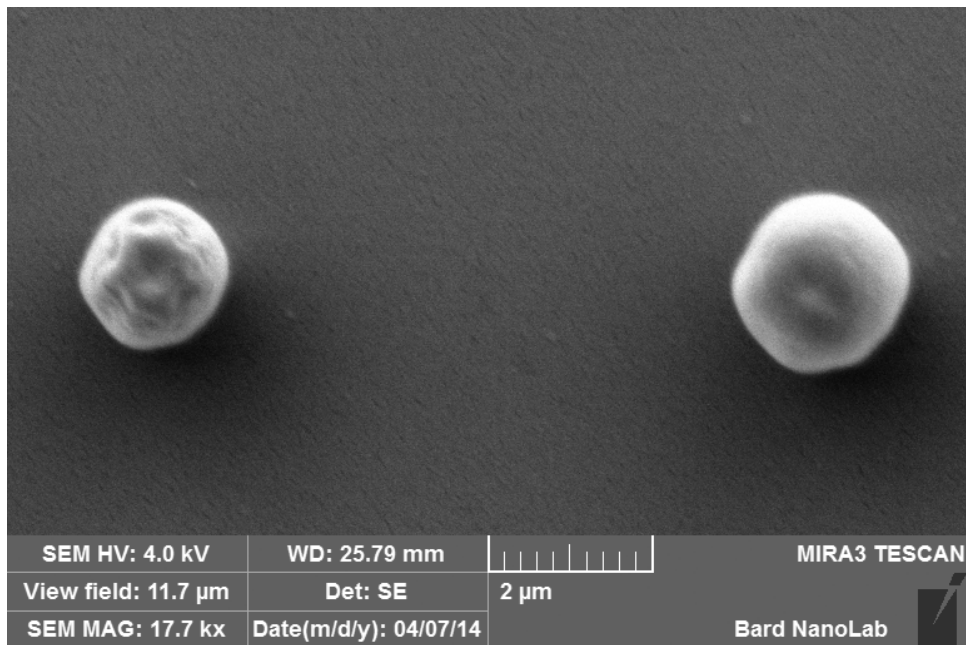


Figure C.4: SEM Image of Double-Dot Experiment #4

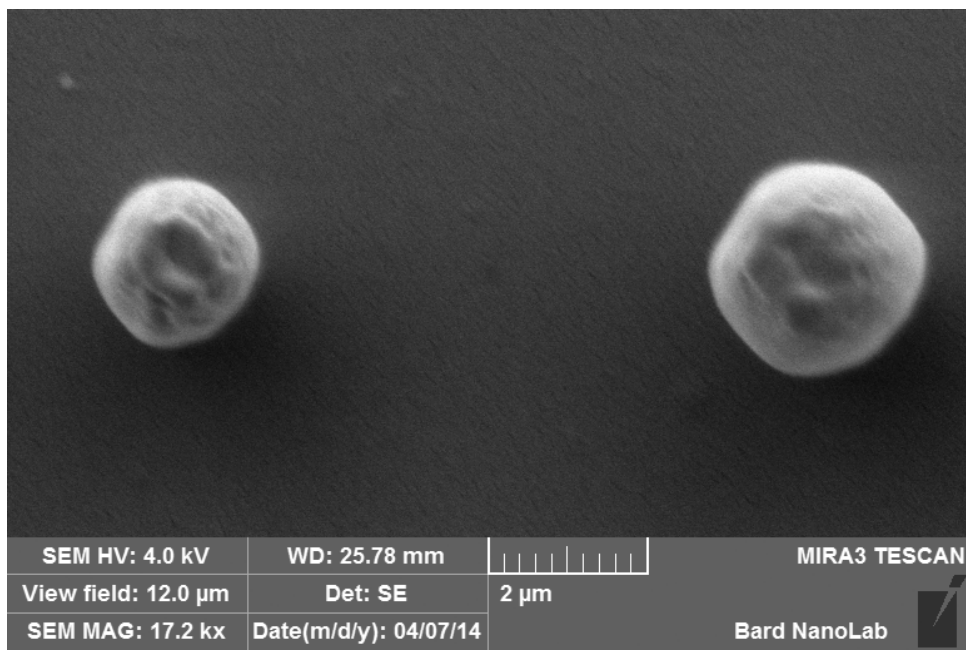


Figure C.5: SEM Image of Double-Dot Experiment #5

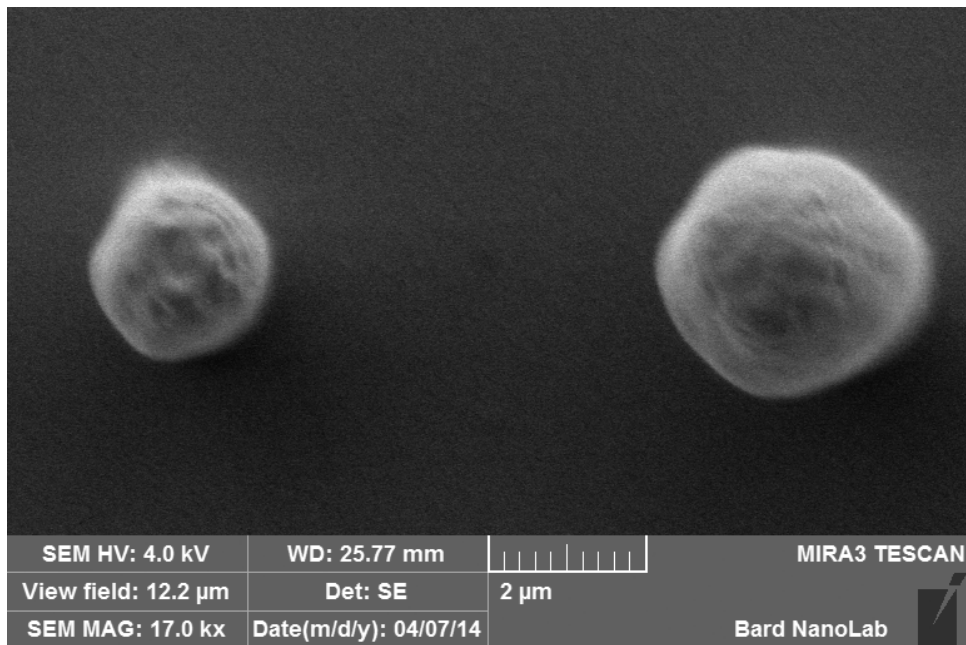


Figure C.6: SEM Image of Double-Dot Experiment #6

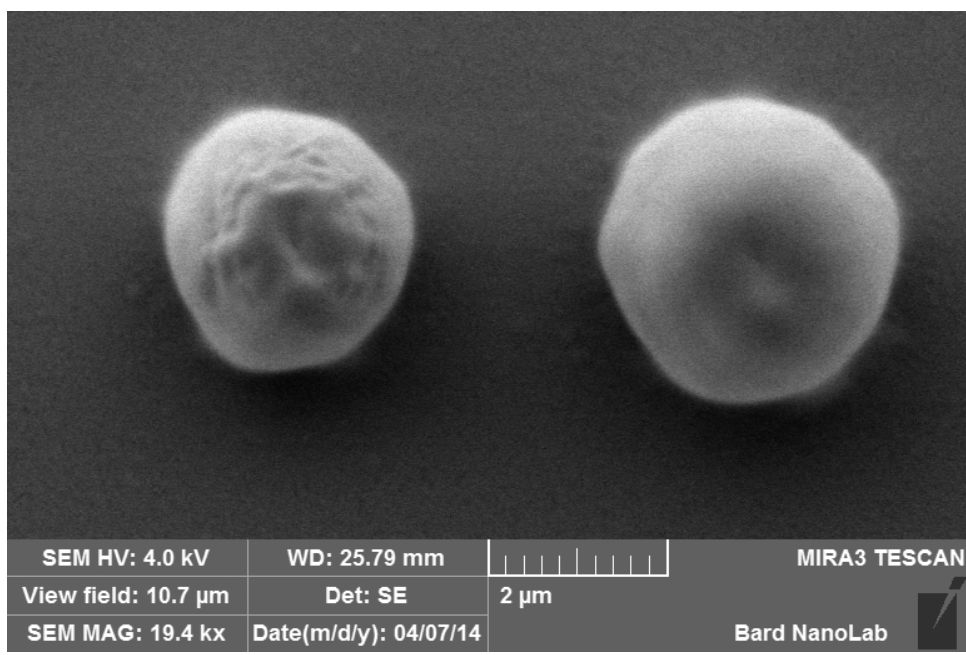


Figure C.7: SEM Image of Double-Dot Experiment #7

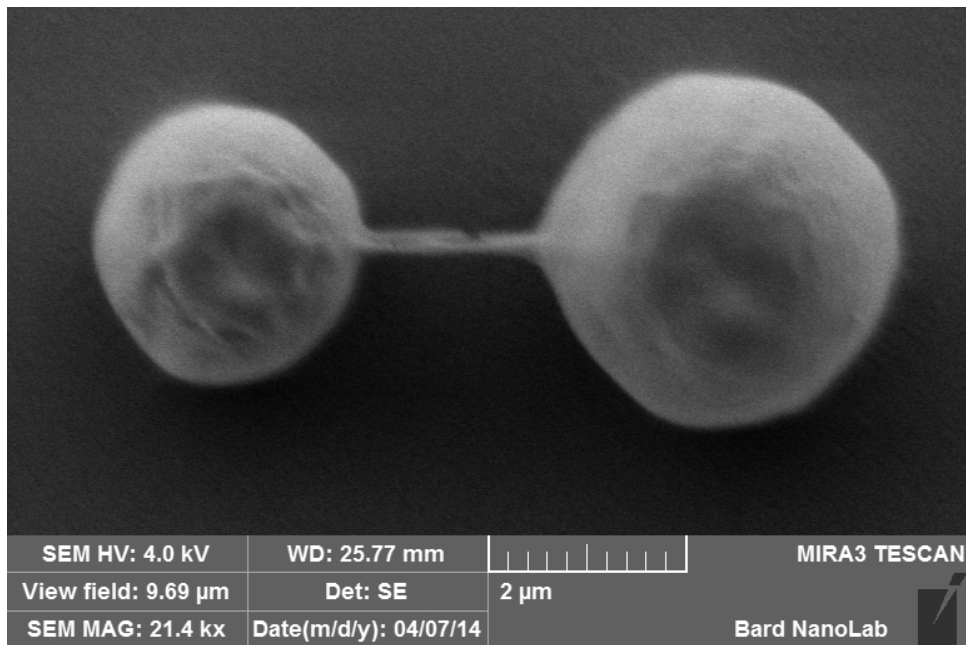


Figure C.8: SEM Image of Double-Dot Experiment #8

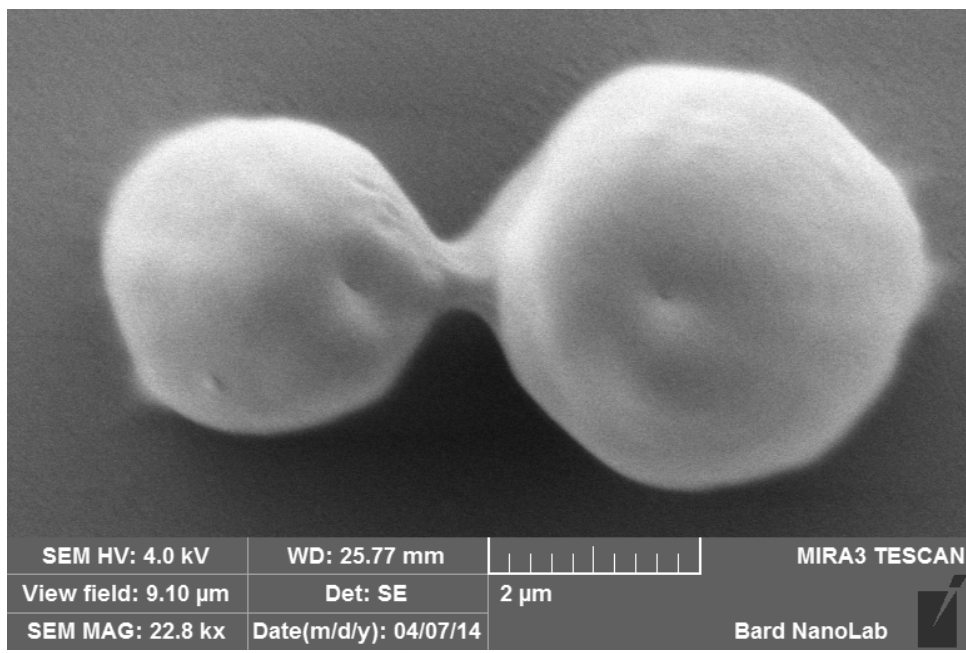


Figure C.9: SEM Image of Double-Dot Experiment #9

Appendix D

Coding in Mathematica

D.1 Parameters

```
(* Experimentally Controlled Variables *)
ExposureTime1 = 0.5; ExposureTime2 = 0.5; HiatusTime = 1; Spacing = 10;

(* Beam Profile Calculation *)
Theta = ArcSin[1.3/1.5]; Lambda = 0.405; W0 =
Lambda/(Pi*Theta); z0 = (Pi*W0^2)/Lambda;(* Beam Profile *)
W[z_] = W0*.Sqrt[1 + (z/z0)^2];(* Beam Radius (um) *)
P = 200; (* Power output of laser (nW) *)
I0 = (2 P)/(Pi*W0^2*10^3); (* I0: Intensity at center (W/m^2) *)

(* Exposure Sink/Source Term *)
m = 400/I0; (* m: Proportionality constant of intensity v.s. change \
in radical *)
d = 0.3; (* d: Proportionality constant of radical decay *)
z = 1; (* z: Axial distance from focal plane (um) *)
Intensity[x_] := I0 (W0/W[z])^2 Exp[-(2*x^2)/W[z]^2]; (* Gaussian *)

Reflection[x_] :=
I0 (W0/W[z])^2 Exp[-(2*x^2)/(400*W[z]^2)]/12 +
I0 (W0/W[z])^2 Exp[-(2*x^2)/(100*W[z]^2)]/12;
```

```

Exposure[x_, pos_] :=
  m (Intensity[x - pos] +
    Reflection[x - pos]); (* Radical generation from exposure *)

(* Probability Density of Polymerization *)
densityP[u_] := 1/(Exp[20 - 25 u] + 1);

(* Initialization *)
M = 400; dx = 20/M; (* M: # of spatial steps; dx: spacial step *)
dt = 0.002; FinalTime1 =
  ExposureTime1 +
  HiatusTime; (* dt: time step; FinalTime: time domain *)
alpha = .2;
cIC[x_] := 1; initc = {}; (* Initiator concentration c initialization \
*)
beta = .1;
uIC[x_] := 0; initu = {}; (* Radical concentration u initialization *)

pIC[x_, s_] :=
  If[x == s, 1,
   0]; initp1 = {}; initp2 = {}; (* Probability Initialization of the \
first exposure *)
initPoly = {};

```

D.2 Initial Conditions

```

For[k = 0, k <= M, k++,
  initu = Append[initu, uIC[k dx]];
  initc = Append[initc, cIC[k dx]];
  initp1 = Append[initp1, pIC[k dx, 5]];
  initp2 = Append[initp2, pIC[k dx, 5 + Spacing]];
  initPoly = Append[initPoly, 0];
]
u = {initu}; c = {initc}; pRight = {initp1}; pLeft = {initp1}; Poly = \
{initPoly};

```

D.3 First Exposure

```
(* First Exposure *)
For[n = 1, n*dt <= FinalTime1, n++, (* Time Domain *)
  cnew = {}; unew = {}; pnewRight = {}; pnewLeft = {};
  For[k = 0, k <= M, k++, (* Spatial Domain *)
    Delta =
      If[n*dt <= ExposureTime1, dt*Exposure[k dx, 5]*c[[n]][[k + 1]], 0];
    cnew = Append[cnew,
      If[0 < k && k < M,
        c[[n]][[k + 1]] +
        If[Poly[[n]][[k + 1]] == 0 || Poly[[n]][[k]] == 0 ||
          Poly[[n]][[k + 2]] == 0, alpha, 0]*
        dt*((c[[n]][[k + 2]] - 2*c[[n]][[k + 1]] +
          c[[n]][[k]])/(dx^2) - c[[n]][[k + 1]] + 1) - Delta,
      If[k == 0,
        c[[n]][[2]] +
        alpha*dt*((c[[n]][[3]] - 2*c[[n]][[2]] + c[[n]][[1]])/(dx^2) -
          c[[n]][[2]] + 1) - Delta, (* Left Boundary *)
        c[[n]][[M]] +
        alpha*dt*((c[[n]][[M + 1]] - 2*c[[n]][[M]] +
          c[[n]][[M - 1]])/(dx^2) - c[[n]][[M]] + 1) - Delta](*
      Right Boundary *)
    ];
    ];
  unew = Append[unew,
    If[0 < k && k < M,
      (1 - d*dt*(u[[n]][[k + 1]] + 1))*u[[n]][[k + 1]] +
      If[Poly[[n]][[k + 1]] == 0 || Poly[[n]][[k]] == 0 ||
        Poly[[n]][[k + 2]] == 0, beta, 0]*
      dt*(u[[n]][[k + 2]] - 2*u[[n]][[k + 1]] +
        u[[n]][[k]])/(dx^2) + 2*Delta,
    If[k == 0,
      u[[n]][[2]] +
      beta*dt*(u[[n]][[3]] - 2*u[[n]][[2]] + u[[n]][[1]])/(dx^2) +
      2*Delta, (* Left Boundary *)
      u[[n]][[M]] +
      beta*dt*(u[[n]][[M + 1]] - 2*u[[n]][[M]] +
        u[[n]][[M - 1]])/(dx^2) + 2*Delta](* Right Boundary *)
    ];
  ];
]
```

```

pnewRight = Append[pnewRight,
  If[0 < k && k < M,
    pRight[[n]][[k + 1]]*(1 - densityP[u[[n]][[k + 1]]]) +
    pRight[[n]][[k]]*densityP[u[[n]][[k]]],  

  If[k == 0,  

    pRight[[n]][[2]]*(1 - densityP[u[[n]][[2]]]) +
    pRight[[n]][[1]]*densityP[u[[n]][[1]]], (* Left Boundary *)
    pRight[[n]][[M]]*(1 - densityP[u[[n]][[M]]]) +
    pRight[[n]][[M - 1]]*densityP[u[[n]][[M - 1]]]] (*
  Right Boundary *)
  ]
];
pnewLeft = Append[pnewLeft,
  If[0 < k && k < M,
    pLeft[[n]][[k + 1]]*(1 - densityP[u[[n]][[k + 1]]]) +
    pLeft[[n]][[k + 2]]*densityP[u[[n]][[k + 2]]],  

  If[k == 0,  

    pLeft[[n]][[2]]*(1 - densityP[u[[n]][[2]]]) +
    pLeft[[n]][[3]]*densityP[u[[n]][[3]]], (* Left Boundary *)
    pLeft[[n]][[M]]*(1 - densityP[u[[n]][[M]]]) +
    pLeft[[n]][[M + 1]]*densityP[u[[n]][[M + 1]]]] (*
  Right Boundary *)
  ]
];
c = Append[c, cnew]; u = Append[u, unew];
pRight = Append[pRight, pnewRight]; pLeft = Append[pLeft, pnewLeft];
(* Expected value for the boundaries in terms of box number *)
leftExpect = Sum[pnewLeft[[i]]*i, {i, 1, Length[pnewLeft]}];
rightExpect = Sum[pnewRight[[i]]*i, {i, 1, Length[pnewRight]}];
Polynew = {};
For[k = 1, k <= M + 1, k++,
  Polynew =
    Append[Polynew,
      If[(leftExpect < k && k < rightExpect) || Poly[[-1]][[k]] == 1, 1,
        0]]
  ];
Poly = Append[Poly, Polynew];
]
FirstDotSize = Total[Poly[[-1]]]

```

D.4 Second Exposure

```
(* Second Exposure *)
FinalTime2 = FinalTime1 + ExposureTime2 + 1;
pRight = {initp2}; pLeft = {initp2};
IndexOffSet = FinalTime1/dt;
For[n = IndexOffSet + 1, n*dt <= FinalTime2, n++, (* Time Domain *)
  cnew = {}; unew = {}; pnewRight = {}; pnewLeft = {};
  For[k = 0, k <= M, k++, (* Spatial Domain *)
    Delta =
      If[n*dt <= FinalTime1 + ExposureTime2,
       dt*Exposure[k dx, 5 + Spacing]*c[[n]][[k + 1]], 0];
    cnew = Append[cnew,
      If[0 < k && k < M,
       c[[n]][[k + 1]] +
       If[Poly[[n]][[k + 1]] == 0 || Poly[[n]][[k]] == 0 ||
          Poly[[n]][[k + 2]] == 0, alpha, 0]*
         dt*(c[[n]][[k + 2]] - 2*c[[n]][[k + 1]] + c[[n]][[k]])/(dx^2) -
         Delta,
       If[k == 0,
        c[[n]][[2]] +
        alpha*dt*(c[[n]][[3]] - 2*c[[n]][[2]] + c[[n]][[1]])/(dx^2) -
        Delta, (* Left Boundary *)
        c[[n]][[M]] +
        alpha*dt*(c[[n]][[M + 1]] - 2*c[[n]][[M]] +
        c[[n]][[M - 1]])/(dx^2) - Delta] (* Right Boundary *)
      ]
    ];
    unew = Append[unew,
      If[0 < k && k < M,
       (1 - d*dt*(u[[n]][[k + 1]] + 1))*u[[n]][[k + 1]] +
       If[Poly[[n]][[k + 1]] == 0 || Poly[[n]][[k]] == 0 ||
          Poly[[n]][[k + 2]] == 0, beta, 0]*
         dt*(u[[n]][[k + 2]] - 2*u[[n]][[k + 1]] +
         u[[n]][[k]])/(dx^2) + 2*Delta,
       If[k == 0,
        u[[n]][[2]] +
        beta*dt*(u[[n]][[3]] - 2*u[[n]][[2]] + u[[n]][[1]])/(dx^2) +
        2*Delta, (* Left Boundary *)
        u[[n]][[M]] +
        beta*dt*(u[[n]][[M + 1]] - 2*u[[n]][[M]] +
        u[[n]][[M - 1]])/(dx^2) - 2*Delta] (* Right Boundary *)
      ]
    ];
  ]
];
```

```

        u[[n]][[M - 1]]]/(dx^2) + 2*Delta] (* Right Boundary *)
    ]
];
pnewRight = Append[pnewRight,
  If[0 < k && k < M,
    pRight[[n - IndexOffSet]][[
      k + 1]]*(1 - densityP[u[[n]][[k + 1]]]) +
    pRight[[n - IndexOffSet]][[k]]*densityP[u[[n]][[k]]],
  If[k == 0,
    pRight[[n - IndexOffSet]][[2]]*(1 - densityP[u[[n]][[2]]]) +
    pRight[[n - IndexOffSet]][[1]]*densityP[u[[n]][[1]]], (*
    Left Boundary *)
    pRight[[n - IndexOffSet]][[M]]*(1 - densityP[u[[n]][[M]]]) +
    pRight[[n - IndexOffSet]][[M - 1]]*densityP[u[[n]][[M - 1]]]] (*
    Right Boundary *)
  ]
];
pnewLeft = Append[pnewLeft,
  If[0 < k && k < M,
    pLeft[[n - IndexOffSet]][[
      k + 1]]*(1 - densityP[u[[n]][[k + 1]]]) +
    pLeft[[n - IndexOffSet]][[k + 2]]*densityP[u[[n]][[k + 2]]],
  If[k == 0,
    pLeft[[n - IndexOffSet]][[2]]*(1 - densityP[u[[n]][[2]]]) +
    pLeft[[n - IndexOffSet]][[3]]*densityP[u[[n]][[3]]], (*
    Left Boundary *)
    pLeft[[n - IndexOffSet]][[M]]*(1 - densityP[u[[n]][[M]]]) +
    pLeft[[n - IndexOffSet]][[M + 1]]*densityP[u[[n]][[M + 1]]]] (*
    Right Boundary *)
  ]
];
c = Append[c, cnew]; u = Append[u, unew];
pRight = Append[pRight, pnewRight]; pLeft = Append[pLeft, pnewLeft];
(* Expected value for the boundaries in terms of box number *)
leftExpect = Sum[pnewLeft[[i]]*i, {i, 1, Length[pnewLeft]}];
rightExpect = Sum[pnewRight[[i]]*i, {i, 1, Length[pnewRight]}];
Polynew = {};
For[k = 1, k <= M + 1, k++,
  Polynew =
    Append[Polynew,

```

```

If[(leftExpect < k && k < rightExpect) || Poly[[-1]][[k]] == 1, 1,
  0]
];
Poly = Append[Poly, Polynew];
]
SecondDotSize = Total[Poly[[-1]]] - FirstDotSize
PercentIncrease = (SecondDotSize - FirstDotSize)/FirstDotSize // N

```

D.5 Showing the Result

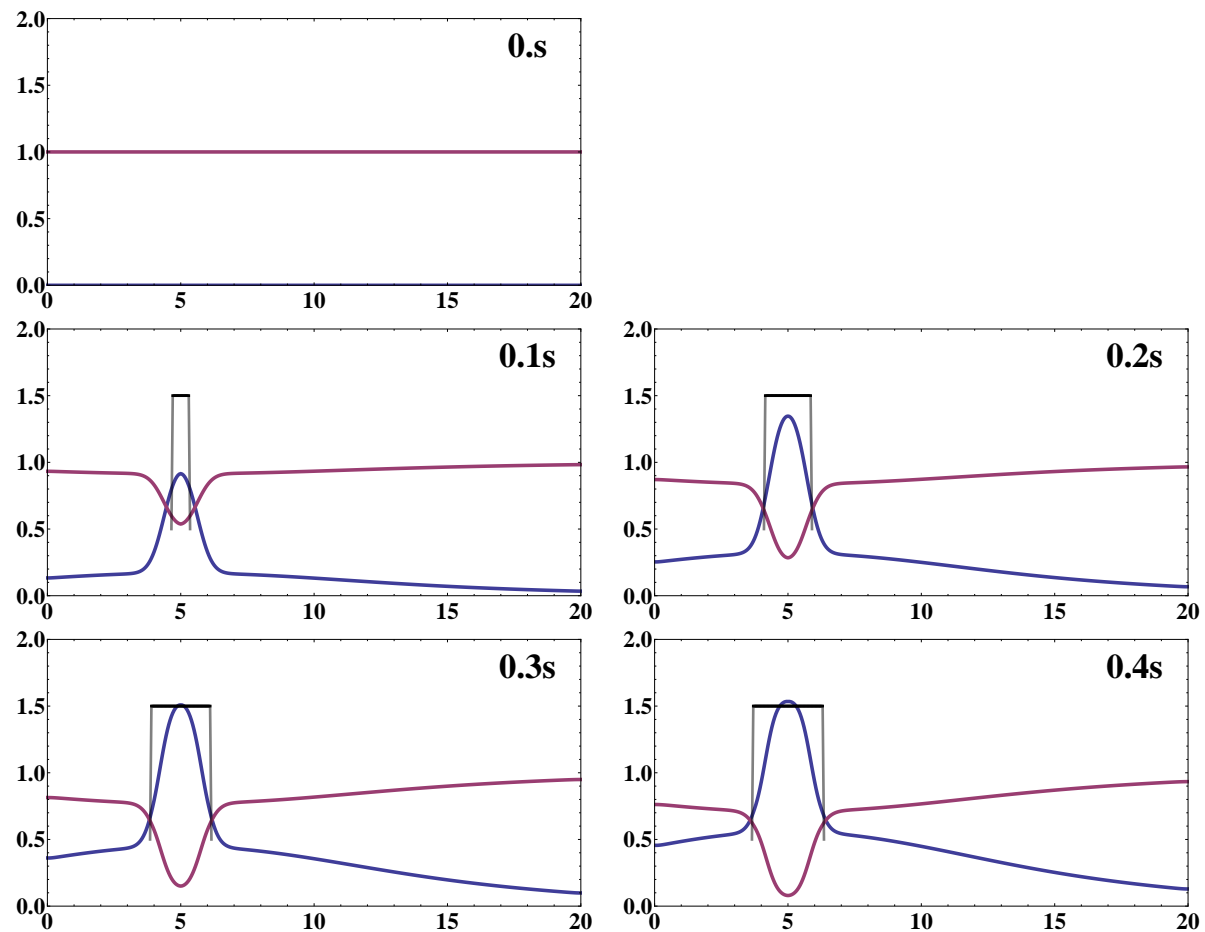
```

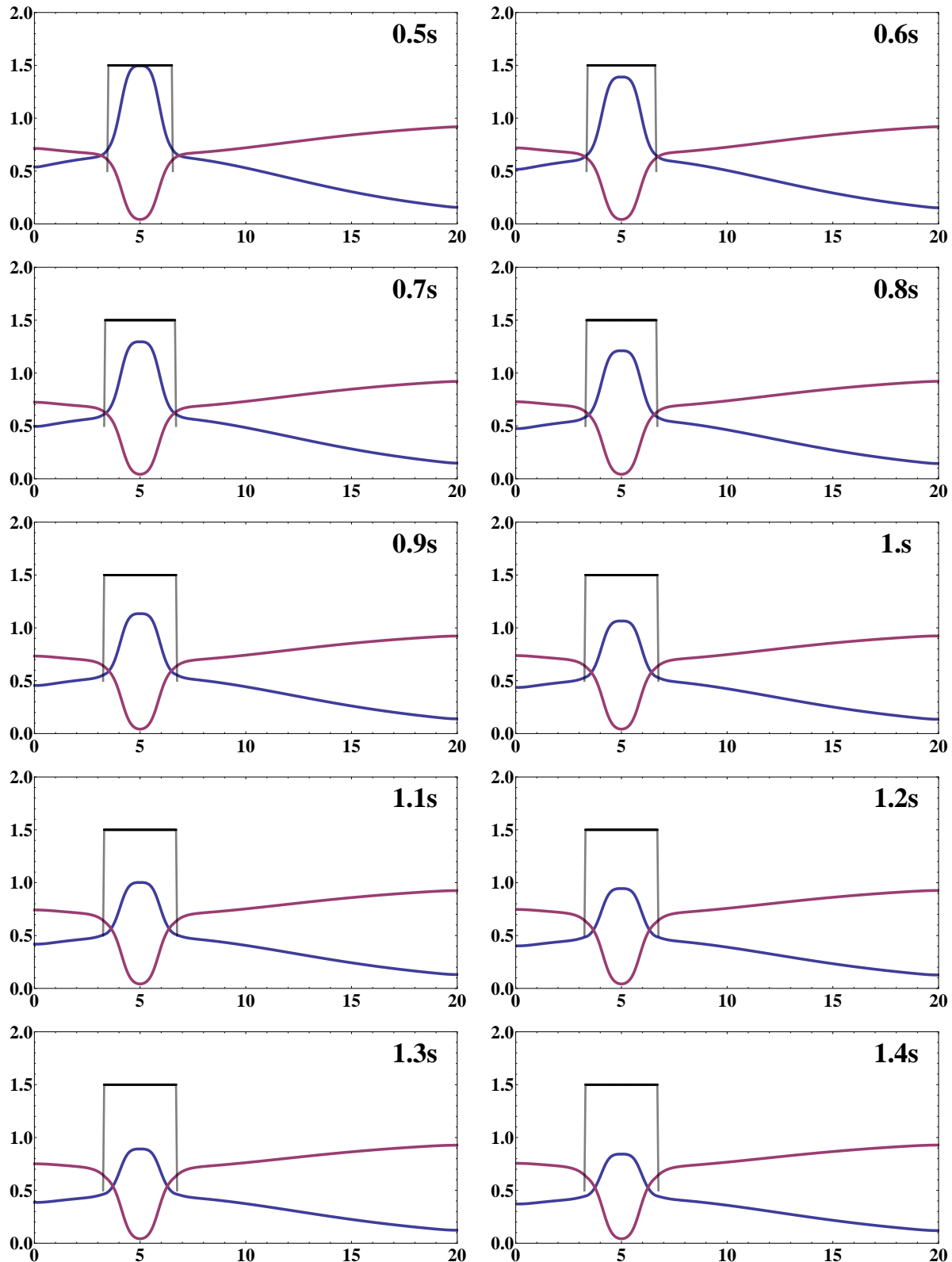
Manipulate[
 Show[
  ListLinePlot[
   {
    Table[{20 (i - 1)/(Length[u[[n]]] - 1), u[[n]][[i]]}, {i, 1,
      Length[u[[n]]}],
    Table[{20 (i - 1)/(Length[c[[n]]] - 1), c[[n]][[i]]}, {i, 1,
      Length[c[[n]]}]
   },
   Axes -> False, Frame -> True, PlotRange -> {{0, 20}, {0, 4/2}},
   ImageSize -> 800, AspectRatio -> 1/2, PlotStyle -> Thickness[1/150],
   Epilog -> {Text[
     Style[ToString[(n - 1)*dt] <> "s", Bold, 48], {18, 1.8}]},
   LabelStyle -> {Bold, 32}
  ],
  ListLinePlot[
   Table[{20 (i - 1)/(Length[Poly[[n]]] - 1),
     Poly[[n]][[i]] + 1/2}, {i, 1, Length[Poly[[n]]]}],
   PlotStyle -> Thickness[1/200],
   ColorFunction -> {Function[{x, y},
     If[y == 1, Black, RGBColor[0, 0, 0]]]}
  ]
 ],
 {n, 1, Length[c], 1}
]

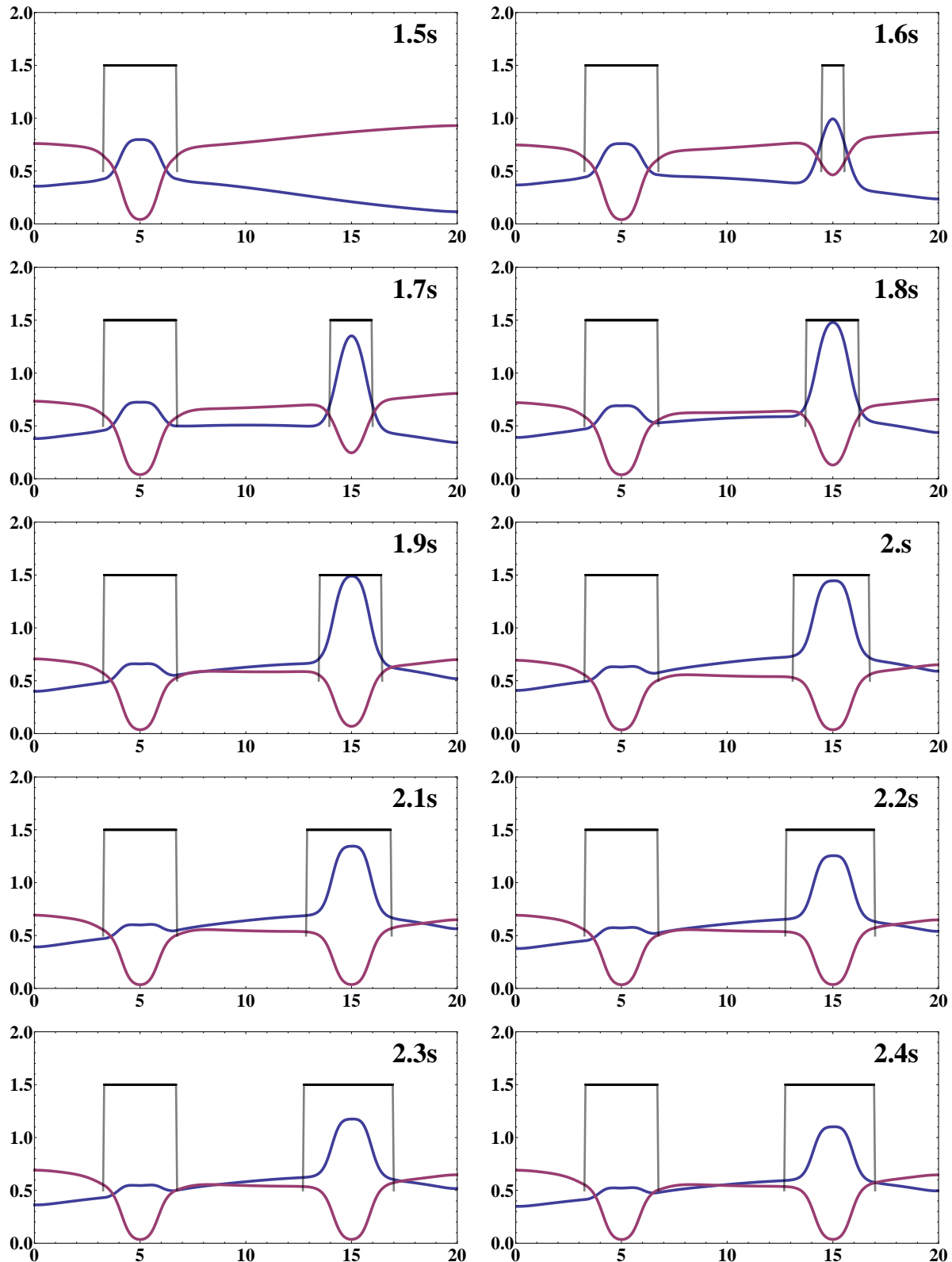
```

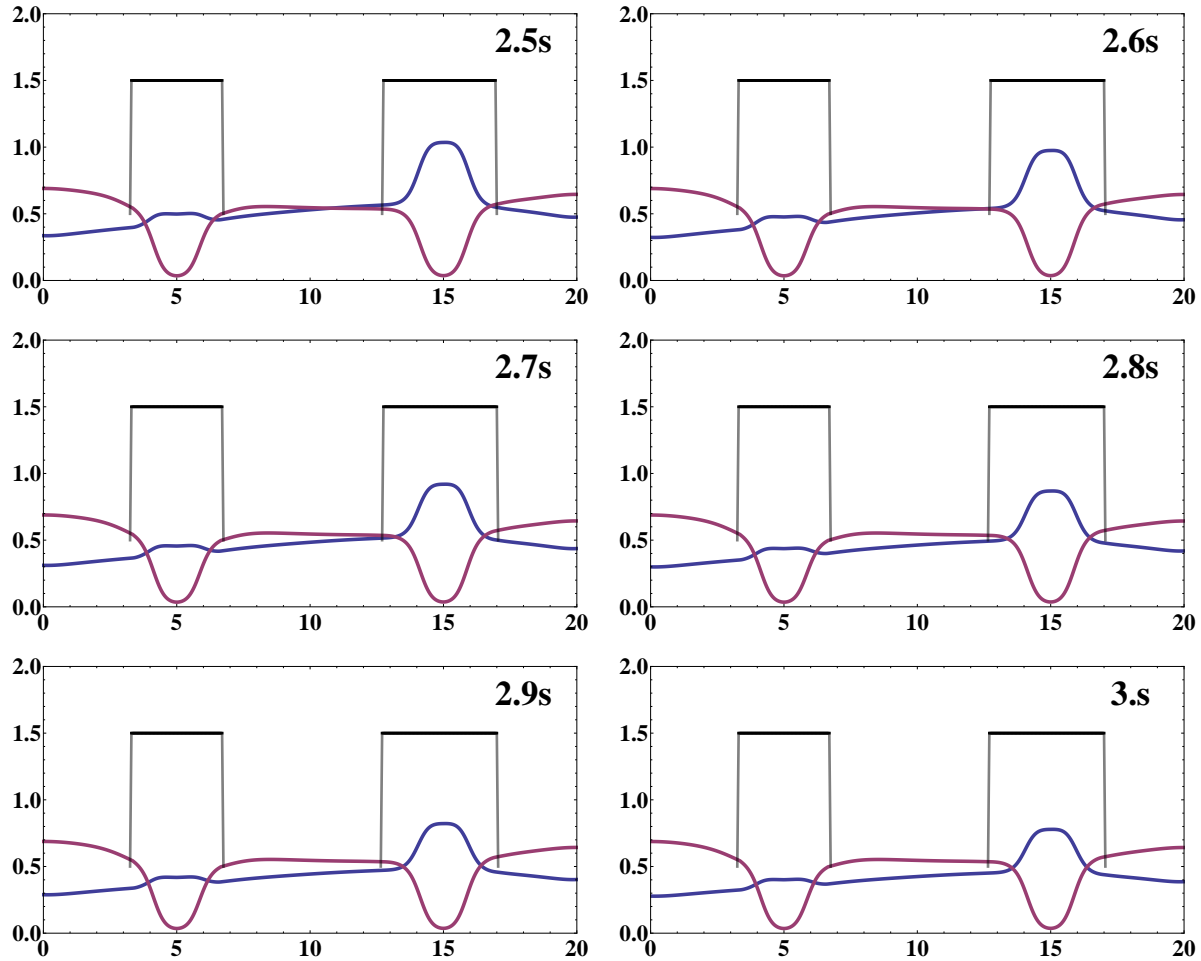
Appendix E

Sample Simulation









Appendix F

General Solutions to $y' = ky(1 - y)$

We first rewrite the differential equation into

$$\frac{dy}{dx} - ky = -ky^2. \quad (\text{F.1})$$

Let $u = y^{-1}$, then $y = u^{-1}$, thus

$$\frac{dy}{du} = -u^{-2}. \quad (\text{F.2})$$

By Chain Rule, it follows that

$$\frac{dy}{dx} = \frac{dy}{du} \cdot \frac{du}{dx} = -u^{-2} \cdot \frac{du}{dx}. \quad (\text{F.3})$$

Substitute (F.3) into (F.1), we obtain

$$-u^{-2} \cdot \frac{du}{dx} - ku^{-1} = -ku^{-2}. \quad (\text{F.4})$$

Multiply both sides by $-u^2$, we obtain

$$\frac{du}{dx} + ku = k. \quad (\text{F.5})$$

Let the integrating factor $\mu(x) = e^{\int k dx} = e^{kx}$. We multiply both sides by the integrating factor, then integrate over x , we get

$$\int \left(e^{kx} \cdot \frac{du}{dx} + ke^{kx} \cdot u \right) dx = \int ke^{kx} dx. \quad (\text{F.6})$$

The integrand of the left-hand side is the derivative of $e^{kx} \cdot u(x)$, and the integrand of the right-hand side is the derivative of e^{kx} . Thus we have

$$e^{kx} \cdot u(x) = e^{kx} + C. \quad (\text{F.7})$$

We solve for $u(x)$, and get

$$u(x) = 1 + e^{c-kx}. \quad (\text{F.8})$$

Thus the general solution to $y(x)$, in closed form, is

$$y(x) = \frac{1}{1 + e^{c-kx}}, \quad (\text{F.9})$$

where c and k are constants, and $k > 0$.

Bibliography

- [Abe62] I. D. Abella. Optical double-photon absorption in cesium vapor. *Phys. Rev. Lett.*, 9(11):453–455, Dec 1962.
- [Air35] G. B. Airy. On the diffraction of an object-glass with circular aperture. *Transactions of the Cambridge Philosophical Society*, 5:283–291, 1835.
- [Far82] Stanley J. Farlow. *Partial Differential Equations for Scientists and Engineers*. Dover Publications, Inc., 1982.
- [FW13] Joachim Fischer and Martin Wegener. Three-dimensional optical laser lithography beyond the diffraction limit. *Laser and Photonics Reviews*, 7(1):22–44, 2013.
- [IKT⁺08] Kazuyoshi Itoga, Jun Kobayashi, Yukiko Tsuda, Masayuki Yamato, and Teruo Okano. Second-generation maskless photolithography device for surface micropatterning and microfluidic channel fabrication. *Analytical Chemistry*, 80(4):1323–1327, 2008. PMID: 18211096.
- [Jae02] Richard C. Jaeger. *Introduction to Microelectronic Fabrication*, volume 5 of *Modular Series on Solid State Devices*, chapter 2 Lithography, pages 17–42. Prentice Hall, 2nd edition, 2002.
- [KOM⁺13] Michelle L. Kovarik, Douglas M. Orloff, Adam T. Melvin, Nicholas C. Dobes, Yuli Wang, Alexandra J. Dickinson, Philip C. Gach, Pavak K. Shah, and Nancy L. Allbritton. Micro total analysis systems: Fundamental advances and applications in the laboratory, clinic, and field. *Analytical Chemistry*, 85(2):451–472, 2013.
- [Moo65] Gordon E. Moore. Cramming more components onto integrated circuits. *Electronics*, 1965.

- [PY05] Michael F. Perry and Gerald W. Young. A mathematical model for photopolymerization from a stationary laser light source. *Macromolecular Theory and Simulations*, 14(1):26–39, 2005.
- [RC97] P. Rai-Choudhury, editor. *Handbook of Microlithography, Micromachining, and Microfabrication*, volume 1, chapter 2 Electron beam lithography, pages 139–250. Society of Photo-Optical Instrumentation Engineers, March 1997.
- [Rev84] D. Revus. *Markov Chains*. Elsevier, 1984.
- [Rub74] Robert Rubinstein. Examples of nonsolvable partial differential equations. *Trans. Amer. Math. Soc.*, 199:123–129, 1974.
- [Sig13] Sigma-Aldrich. *Diethyl ether, Material Safety Data Sheet*, 5.2 edition, August 2013.
- [ST91] Bahaa E. Saleh and Malvin Carl Teich. *Fundamentals of Photonics*. Wiley series in pure and applied optics. Wiley, 1991.
- [Sza10] Csilla Szabo. *Markov Models for Actin Polymer Dynamics and Cell Membrane Protrusion*. PhD thesis, Rensselaer Polytechnic Institute, May 2010.
- [TBP⁺11] Giovanna Tomaiuolo, Mario Barra, Valentina Preziosi, Antonio Cassinese, Bruno Rotoli, and Stefano Guido. Microfluidics analysis of red blood cell membrane viscoelasticity. *Lab Chip*, 11:449–454, 2011.
- [Tho95] J. W. Thomas. *Numerical Differential Equations: Finite Difference Methods*. Springer, 1995.
- [ZNWS13] Yi Zheng, John Nguyen, Chen Wang, and Yu Sun. Electrical measurement of red blood cell deformability on a microfluidic device. *Lab Chip*, 13:3275–3283, 2013.
- [ZRM⁺03] Dong S. Zhao, Binayak Roy, Matthew T. McCormick, Werner G. Kuhr, and Sara A. Brazill. Rapid fabrication of a poly(dimethylsiloxane) microfluidic capillary gel electrophoresis system utilizing high precision machining. *Lab Chip*, 3:93–99, 2003.